Cerebral Cortex, 2019;00: 1–20

doi: 10.1093/cercor/bhz103
Advance Access Publication Date: 26 June 2019
Original Article

ORIGINAL ARTICLE

PTEN Activity Defines an Axis for Plasticity at Cortico-Amygdala Synapses and Influences Social Behavior

Cristina Sánchez-Puelles[1,2,9], María Calleja-Felipe[1], Alberto Ouro[1], Ghassen Bougamra[1], Ana Arroyo[1], Ibai Diez[3], Asier Erramuzpe[3], Jesús Cortés[3,4], José Martínez-Hernández[5], Rafael Luján[5], Marta Navarrete[2,9], César Venero[6], Andrew Chan[7], Miguel Morales[1], José A. Esteban[2,*] and Shira Knafo[1,4,8,*]

[1]Molecular Cognition Laboratory, Biophysics Institute, Consejo Superior de Investigaciones Cientificas (CSIC)-University of the Basque Country (UPV)/Euskal Herriko University (EHU), Campus Universidad del País Vasco, 48940 Leioa, Spain, [2]Department of Molecular Neurobiology, Centro de Biología Molecular Severo Ochoa, CSIC/Universidad Autónoma de Madrid, 28049 Madrid, Spain, [3]Computational Neuroimaging Laboratory, Biocruces Health Research Institute, 48903 Barakaldo, Spain, [4]Ikerbasque, Basque Foundation for Science, 48013 Bilbao, Spain, [5]Synaptic Structure Laboratory, Instituto de Investigación en Discapacidades Neurológicas, Departamento Ciencias Médicas, Facultad de Medicina, Universidad Castilla–La Mancha, 02008 Albacete, Spain, [6]Department of Psychobiology, Universidad Nacional de Educación a Distancia, 28040 Madrid, Spain, [7]School of Biomedical Sciences, The Chinese University of Hong Kong, Hong Kong Special Administrative Region, China, [8]Department of Physiology and Cell Biology and National Institute of Biotechnology in the Negev, Faculty of Health Sciences, Ben-Gurion University of the Negev, Beer-Sheva, 8410501 Israel and [9]Current address: Instituto Cajal, CSIC, 28002 Madrid, Spain

Address correspondence to Shira Knafo, Department of Physiology and Cell Biology, Faculty of Health Sciences, Ben-Gurion University of the Negev, Beer-Sheva, Israel. Email: shirak@post.bgu.ac.il or Jose A. Esteban, Department of Molecular Neurobiology, Centro de Biología Molecular Severo Ochoa, CSIC/Universidad Autónoma de Madrid, 28049 Madrid, Spain. Email: jaesteban@cbm.csic.es

Abstract

Phosphatase and tensin homolog on chromosome 10 (PTEN) is a tumor suppressor and autism-associated gene that exerts an important influence over neuronal structure and function during development. In addition, it participates in synaptic plasticity processes in adulthood. As an attempt to assess synaptic and developmental mechanisms by which PTEN can modulate cognitive function, we studied the consequences of 2 different genetic manipulations in mice: presence of additional genomic copies of the *Pten* gene ($Pten^{tg}$) and knock-in of a truncated *Pten* gene lacking its PDZ motif (Pten-ΔPDZ), which is required for interaction with synaptic proteins. $Pten^{tg}$ mice exhibit substantial microcephaly, structural hypoconnectivity, enhanced synaptic depression at cortico-amygdala synapses, reduced anxiety, and intensified social

interactions. In contrast, Pten-ΔPDZ mice have a much more restricted phenotype, with normal synaptic connectivity, but impaired synaptic depression at cortico-amygdala synapses and virtually abolished social interactions. These results suggest that synaptic actions of PTEN in the amygdala contribute to specific behavioral traits, such as sociability. Also, PTEN appears to function as a bidirectional rheostat in the amygdala: reduction in PTEN activity at synapses is associated with less sociability, whereas enhanced PTEN activity accompanies hypersocial behavior.

Key words: autism, imaging, long-term depression, long-term potentiation, PI3 kinase

Phosphatase and tensin homolog on chromosome 10 (PTEN) was originally discovered as a tumor suppressor protein (Li et al. 1997; Liaw et al. 1997), and it is now known to be a major regulator of key cellular events, including survival, proliferation, and growth (Chow et al. 2009; Gregorian et al. 2009; Amiri et al. 2012). PTEN and phosphatidylinositol-3-kinase (PI3K) bidirectionally control the intracellular levels of phosphatidylinositol-(3,4,5)-triphosphate (PIP_3), an important signaling molecule that promotes cell growth and survival (Cantley 2002). As a negative regulator of the PI3K-PIP_3 pathway, PTEN restrains cell proliferation during embryogenesis and in adulthood (Stiles et al. 2004).

PTEN is widely expressed in the central nervous system throughout development, both in neurons and glia (Cai et al. 2009; González-Fernández et al. 2018). Thus, some of the neurological manifestations provoked by PTEN mutation may derive from aberrant neuronal growth during brain development. In fact, mice with PTEN deficiency develop larger neurons, with more complex dendritic and axonal projections. This phenotype is accompanied by the appearance of abnormally large and abundant synapses (Luikart et al. 2011; Pun Raymund et al. 2012; Williams et al. 2015), giving rise to a structural hyperconnectivity. Nevertheless, PTEN is also expressed at mature synapses in the cerebral cortex and hippocampus (Perandones et al. 2004), and the PI3K/PTEN pathway is essential for some important aspects of synaptic function and plasticity (Man et al. 2003; Opazo et al. 2003; Wang et al. 2006; Peineau et al. 2007; Arendt et al. 2010; Jurado et al. 2010; Cuesto et al. 2011; Sperow et al. 2012; Takeuchi et al. 2013; Arendt et al. 2014; Knafo et al. 2016). Specifically, PI3K activation favors the formation of the PIP_3 required for AMPA receptor (AMPAR) accumulation at synapses (Arendt et al. 2010), whereas PIP_3 down-regulation by PTEN favors AMPAR endocytosis and synaptic depression (Jurado et al. 2010). Accordingly, the performance of a variety of conditional PTEN knockout (KO) mice in some cognitive tasks is impaired (Kwon et al. 2006; Lugo et al. 2014; Huang et al. 2016), evidence that neuronal PTEN is critical to maintain cognitive function. However, it is often challenging to determine specific mechanistic links between PTEN deficiency and its cognitive consequences. On the one hand, PTEN loss of function is likely to trigger pleiotropic alterations affecting multiple signaling pathways within the neuron. On the other hand, both developmental and synapse-specific actions of PTEN may contribute to the observed phenotypes (Knafo and Esteban 2017).

In order to start evaluating distinct roles of PTEN in cognitive behavior, we have employed 2 animal models. First, as a gain-of-function approach, we studied mice carrying additional genomic copies of *Pten* ($Pten^{tg}$). These animals display moderate PTEN overexpression, which dampens PIP_3 signaling and protects them from cancer development (Garcia-Cao et al. 2012; Ortega-Molina et al. 2012). This is the opposite genetic manipulation to that of PTEN KO mice, and therefore, it may shed light on the capacity of the PI3K/PTEN pathway to act as a signaling rheostat for the modulation of neuronal activity. Second, we have used a knock-in mouse line bearing a truncated *Pten* gene that lacks the C-terminal PDZ-binding motif (Pten-ΔPDZ). Total levels of PTEN protein and global activation of the PIP_3 pathway are normal in these animals (Knafo et al. 2016). However, this PDZ motif is required for PTEN recruitment to synapses during plasticity events (Jurado et al. 2010; Knafo et al. 2016). Therefore, this truncated PTEN protein would be unable to engage in synapse-specific mechanisms. Additional alterations in developmental programs or other non-synaptic functions of PTEN cannot be completely ruled out in these animals, but we expect that at least synaptic phenotypes will be present (as a reference, a recent report did not find overt developmental deficits in the mammary glands in mice with the same genetic manipulation; Yan et al. 2018). It is also worth noting that these 2 animal models ($Pten^{tg}$ and Pten-ΔPDZ) do not represent opposite genetic manipulations. One of them involves overexpression, and the other one constitutes a partial loss-of-function knock-in. Nevertheless, we believe they can illustrate different cellular and physiological functions of PTEN when studied in parallel. Using these animals, we have carried out a combination of morphological, electrophysiological, and behavioral experiments. For these studies, we have focused on the amygdala, for which well-defined synaptic correlates of emotional learning and memory have been proposed (Paz and Pare 2013). In addition, dysfunction of amygdala circuits is associated to social impairment (Blair 2013) and intellectual disability (Aincy et al. 2018). By comparing the synaptic physiology and behavioral phenotypes of $Pten^{tg}$ and Pten-ΔPDZ animals, we propose that PTEN activity at synapses defines an axis for the magnitude of long-term synaptic depression at the cortico-amygdala circuit, with bidirectional consequences for social behavior.

Materials and Methods

All the experiments carried out here were performed blind to the conditions, and the results were analyzed with no prior information about the experimental status of the animals. All biosafety procedures and animal care protocols were approved by the bioethics committee of the Consejo Superior de Investigaciones Cientificas, and they were performed in accordance with the guidelines set out in the European Community Council Directive (2010/63/EU).

Mice

Male and female mice aged 6–12 months old were used in these studies, with the exception of the ultrasonic vocalization (USV) experiments, in which the mice used were 3–12 days old. Animals were housed in 500 cm^3 type 2 L cages (maximum 5 animals per cage) under standard conditions of temperature (22 ± 1 °C) and humidity (40–60%) and on a 12 h light/dark cycle (lights on at 8:00, with 30 min of dawn/sunset).

(1) $Pten^{tg}$ mice were generated by bacterial artificial chromosome (BAC) transgenesis on a C57BL6/CBA genetic background (75%:25%), as previously described (Ortega-Molina et al. 2012). Wild-type (WT) littermates were used as controls in each of the experiments involving transgenic mice. At weaning, the mice were genotyped from tail biopsies by means of polymerase chain reaction (PCR) using the primers: forward-T7: 5′-CCGCTAATACGACTCACTATAGGG-3′ and reverse-T7: 5′-TCATCTCGGCTCCATCGTTT-3′.

(2) The *Pten*$^{tm(Q399stop)amc}$ (abbreviated as Pten-ΔPDZ) knock-in mouse strain was generated by homologous recombination in iTL1 129S6/SvEvBrdTac(129Sv)-derived embryonic stem cells. The PDZ-binding domain was deleted by substituting codon 399 (CAA) with a stop codon (TAA), as previously described (Knafo et al. 2016). The chimeric founders were crossed once with C57BL/6J mice (stock#664; The Jackson Laboratory) to generate heterozygous offspring and then with B6.FVB-Tg(EIIa-cre)C5379Lmgd/J mice (stock#3724; The Jackson Laboratory) to remove the neomycin gene cassette. The progeny were backcrossed 10 generations to a C57BL/6 background, and homozygous mice were generated by crossing heterozygous animals. WT littermates were used as controls. Genotyping was carried out by PCR using the following primers: 5′-GCTGAAGTGGCTGAAGAGCTCTGA-3′ and 5′- TTGAGTGAAACTGATGAGGTATGG-3′. The WT allele yielded a 1545 base pair (bp) fragment while the KO allele generated a 1724 bp product due to the presence of a 179 bp sequence from the knock-in vector following Cre-mediated recombination.

To note, since $Pten^{tg}$ and Pten-ΔPDZ mice have different genetic backgrounds, so they have their corresponding WT littermates used as controls. This may introduce differences in the results across the 2 WT sets, but we believe this is the most appropriate comparison with their corresponding transgenic mice.

Combined Micro-PET/Micro-CT Imaging

High-Resolution Micro-PET-CT

The mice were anesthetized with isofluorane, and positron emission tomography (PET)-computed tomography (CT) scans were acquired with an eXplore Vista PET-CT system 30 min after intravenous injection of 14 MBq ^{18}F-FDG. Reconstructions were obtained with 3D ordered subset expectation maximization (OSEM). The mice were placed prone inside polypropylene tubes (50 mL) that were arranged together in a wooden box with parallel holes. All the animals were placed with their snouts in the same vertical plane and each animal was given a code for future identification. The box containing the mice was then placed in the CT gantry for head scanning, obtaining CT images in a multi-slice CT-scanner (General Electric, EU) using 16 channels by applying 140 kV at 165 mAs/s (Kernel U90). Thin slices (0.625 mm thick) were analyzed 1 mm apart that covered the mouse's entire head. Images were acquired in the axial, coronal, and sagittal planes, and the bone algorithm was applied to better visualize the skull. The field of view was 18 cm, with a 512×512 matrix. Following the scan, the mice were placed in their cages for 35 min to recover from the anesthesia, with ad libitum access to a standard laboratory diet and water. Three-dimensional reconstructions of these images were processed by the volume rendering method.

PET-CT Acquisition Before and After Auditory Fear Conditioning

Prior to conditioning (24 h), each mouse was intravenously injected with 14 MBq of ^{18}F-FDG and 30 min later, a basal PET study was performed to obtain a baseline signal from the brain. On the training (conditioning) day, mice were injected with ^{18}F-FDG 20 min before the beginning of the conditioning session. The mice were then exposed to the conditioning context (180 s) followed by a tone (conditioned stimulus [CS]: 20 s, 2 kHz, 85 dB). After termination of the tone, a footshock (unconditioned stimulus [US]: 0.75 mA, 2 s) was delivered through a stainless steel grid floor. Mice received 4 footshocks with an intertrial interval of 60 s. The mice were then removed from the fear-conditioning box 30 s after the last shock terminated. They were immediately anesthetized with isofluorane for PET scan (Fig. 4*d*). On the next day, mice were injected with ^{18}F-FDG 20 min before the memory retrieval test. For this test, mice were placed into a novel context (same cages but with different walls, floor, and background odor) and after a 3 min baseline period, they were continuously re-exposed to the tone for 5 min (the same characteristics as during conditioning), although without any electric shocks. The animal's behavior was scored by an observer blind to the treatment using a time-sampling procedure every 2 s, and each mouse was scored as either freezing or active at the instant the sample was taken. Freezing was defined as behavioral immobility, except for the movements associated with respiration.

PET-CT Data Analysis

Images were analyzed using Amide (NIH) software, first manually segmenting the mouse skull from the CT image to calculate the intracranial volume and using this brain segmentation as a mask for individual PET normalization, dividing each value of the voxel intensity by the average intensity within the mask. Finally, all voxel intensities were spatially smoothed using a 0.6 mm full width at half maximum isotropic Gaussian kernel. To perform group comparisons in the PET activation maps (WT vs. $Pten^{tg}$), we first coregistered each PET image to its corresponding CT using the Slicer software (https://www.slicer.org/), applying the BRAINS linear transformation from the PET to the CT. Next, all PET images were transformed to a common space using the FMRIB Linear Image Registration Tool transformation (Jenkinson and Smith 2001), incorporated as part of the open-source FSL software. The common space to which all PET images were transformed to was defined by the "In vivo Mouse Brain Atlas" (Bai et al. 2012) (available at http://www.bioeng.nus.edu.sg/cfa/mouse_atlas.html) and by the AtlasGuide (Li et al. 2013). Using these atlases, 6 different regions of interest (ROIs) were defined: the amygdala, the thalamus, the auditory cortex (AC), the frontal cortex, and the dorsal and ventral hippocampus. Group comparisons were performed using Randomize, an FSL tool for nonparametric testing that uses threshold-free cluster enhancement and family-wise error, with a corrected value of $P < 0.05$. After applying Randomize, 6 different brain activity maps were obtained: 2 maps for the recording of basal brain activity ($activity_{WT} > activity_{Pten^{tg}}$ and $activity_{WT} < activity_{Pten^{tg}}$), 2 maps for the activity during conditioning with respect to the basal activity, and 2 maps for the activity during retrieval with respect to basal activity. We next obtained the intersection between each of the 6 maps resulting from Randomize, using the 6 ROIs identified from the atlases to extract all the voxels in each ROI from each of the 6 maps, and we did the same for each mouse. Finally, we calculated the mean activity in each of these regions.

Antibodies

The primary antibodies used in this study were raised against the following: PTEN 138G6 (9559; Cell Signaling), Actin (MAB1501R; Millipore), tGluA1 (AB31232; Abcam), pGluA1 S831 (AB5847; Merck Millipore), pCaMKII Thr286 (Merck Millipore, 1:1000), and tCaMKII (alpha subunit; Sigma-Aldrich, 1:1000).

Unbiased Stereology

Mice were anesthetized with 16% chloral hydrate injected intraperitoneally, and they were perfused with a saline solution (0.9% NaCl) and then with 4% paraformaldehyde (PFA, pH 7.4). The extracted brains were then post-fixed overnight in PFA and cryoprotected in a solution of 3% glycerol ($C_3H_8O_3$: Panreac ref.141339) and 3% ethylene glycol in PB (CH_2OHCH_2OH: Panreac 141316). Serial coronal vibratome sections (40 µm, Leica VT1200S) were Nissl stained with 0.1% cresyl violet (Fluka, Ref. 61123) and mounted on histological glass slides with DPX mount (Sigma). The slices were quantified stereologically according to the Allen Mouse Brain Atlas (2016, Allen Institute for Brain Science, available at mouse.brain-map.org), using a 5× objective lens on a light microscope (Leica DRIV microscope) equipped with a MicroFire digital camera (Optronics) and a motorized stage. The volumes were calculated with the Stereo Investigator software (MicroBrightField) according to the Cavalieri estimator (Blasco et al. 1999). Any incomplete stained or torn section was considered a random event, designated missing, and then accounted for in the stereological estimate using the fractionator principle (Stereo Investigator software v10, MBF Biosciences).

Cell counting was performed in the CA1 (counting frame, 15 × 15; sampling grid, 65 × 65; dissector height, 30 µm; interval, 6) and lateral amygdala (LA) (counting frame, 14 × 14; sampling grid, 45 × 45; dissector height, 30 µm; interval, 2) using the optical fractionator method in the Stereo Investigator software. Cells were marked only if their edges were within the dissector area and they did not intersect forbidden lines. The cells were also marked if they came into focus as the optical plane moved through the height of the dissector. The precision of our stereological counts was determined by the Gunderson coefficient of error equation (Knafo et al. 2009a, 2009b). This method of sampling and the section intervals were tested in a pilot experiment to ensure that the number of cells estimated was representative of their total number.

Electron Microscopy

Mice were anesthetized with an intraperitoneal injection of thiobarbital (346836, Braun) and perfused with a mixture of PFA (4%) and glutaraldehyde (2%) in PB. Their brain was post-fixed in the same solution overnight, and coronal sections were then obtained, which were post-fixed in 1% osmium tetroxide (in 0.1 M cacodylate buffer), dehydrated in ethanol, and embedded in Epon-Araldite. Serial ultrathin sections of the LA and hippocampus were collected on pioloform-coated, single-hole grids and stained with uranyl acetate and lead citrate. The sections were analyzed on a JEM-1010 transmission electron microscope (Jeol) equipped with a side-mounted Mega View III CCD camera (Olympus Soft Imaging System GmBH). The neuropil was sampled randomly and imaged at a magnification of ×75 000, and the length of the postsynaptic density (PSD) was measured with the AnalySIS software (Soft Imaging System GmBH).

Neuronal Morphology and Spine Density

Patch Clamp for Biocytin Cell Filling and Whole-Cell Capacitance Measurement

To analyze neuronal morphology, pyramidal neurons in the LA of acute slices (see below "acute slice preparation") were filled with biocytin using a patch pipette under whole-cell configuration. The external artificial cerebrospinal fluid (ACSF) gassed with 95% O_2 and 5% CO_2 contained 119 mM NaCl, 2.5 mM KCl, 1 mM NaH_2PO_4, 11 mM glucose, 26 mM $NaHCO_3$, 4 mM $MgCl_2$, 4 mM $CaCl_2$, 100 µM picrotoxin, and 2 µM 2-chloroadenosine (pH 7.4). Patch recording pipettes (4–7 MΩ) were filled with an internal solution containing 115 mM $CsMeSO_3$, 20 mM CsCl, 10 mM HEPES, 2.5 mM $MgCl_2$, 4 mM Na_2-ATP, 0.4 mM Na-GTP, 10 mM sodium phosphocreatine, biocytin (10 mg/2 mL; Sigma#B4261), and 0.6 mM EGTA (pH 7.25). After filling, the slices were immersed in 4% PFA, 4% sucrose in PBS overnight at 4 °C, and they were then treated for 48 h at 4 °C with Alexa488-Streptavidin (1:500; S-32254 Thermo Fisher) in blocking solution (5% sucrose, 2% BSA, and 1% Triton X-100 in PBS). Finally, the slices were washed in PBS and mounted in Prolong Antifade Gold (Invitrogen).

Morphometry

Images of neurons were acquired with a 2-photon LSM710 microscope using a 40×/1.30 EC "Plan-Neofluar" Oil DIC M27 objective and the Argon 488 nm laser line, obtaining images of the entire dendritic tree through the tile-scan application. To analyze neuron morphology, image stacks were imported into the Neurolucida software (MicroBrightField Inc.), and the neuronal dendritic trees were 3-dimensionally traced by marking the dendrites and the bifurcation points while focusing up and down in the stack. A Sholl analysis was performed for each neuron by automatically calculating the number of dendritic intersections at 10 µm intervals starting from the soma (Knafo et al. 2009a, 2009b). The number of intersections for each neuron was also calculated as an index of dendrite complexity. Dendrite images were acquired on a confocal LSM510 META microscope using a 63×/1.4 oil Plan-Apochromat M27 objective, with a calculated optimal zoom factor of 3.2 and a z-step of 0.14 µm (voxel size, 75.1 × 75.1 × 136.4 nm). To analyze spine density, the stacks were processed after image acquisition with a 3-dimensional blind deconvolution algorithm to reduce the out-of-focus light using Huygens software (Huygens 4.3.1p2 64b S.V.I.). To measure spine density, image stacks were analyzed with Neurolucida software and the spine density was calculated for each dendrite by dividing the number of spines by the corresponding dendritic length. Spine density was also analyzed as a function of its distance from the soma through a Sholl analysis, dividing the number of spines by the length of the dendritic segment for every 10 µm segment from the soma.

Preparation of Primary Hippocampal Cultures

Dissociated neurons were prepared from E15 embryos obtained from $Pten^{tg}$ dams using standard procedures. As the weight of the $Pten^{tg}$ and WT embryos does not overlap (data not shown), they were distinguished by this parameter and the genotype was later confirmed by PCR. The hippocampi were dissected out and dissociated by mechanical trituration in trypsin (0.25%) and DNAseI (0.1 mg/ml). Neurons were plated on 0.1 mg/mL poly-L-lysine-coated coverslips (14 mm round; Menzel-Gläser) at a final density of 2×10^5 cells/coverslip. The neurons were maintained at 37 °C in an atmosphere of 5% CO_2, and in

Neurobasal medium (Gibco) supplemented with B27 (Gibco) and GlutaMAX (Gibco), for 7 days in vitro (DIV), when the medium was replaced with Neurobasal medium plus B27 without GlutaMAX. To prevent glial proliferation, cultures were treated with cytosine arabinoside (5 µM; Sigma-Aldrich) after incubation for 4 DIV.

Spine Quantification

To visualize dendrites and spines, primary hippocampal neurons were infected at DIV 24 with Sindbis virus to express GFP–Actin. The cells were fixed in 4% PFA for 10 min at room temperature and images were acquired as described for the acquisition of dendrites in the "Morphometry" section. To quantify spines, secondary dendrites were traced in 3 dimensions with Imaris 7.2.0 software and the spines were marked with the measurement tool in the same software. The number of spines was divided by the length of each secondary dendrite to calculate the spine density.

Chemical LTP

PTEN-EGFP and EGFP were expressed in dissociated DIV 21 rat hippocampal neurons using Sindbis pseudovirus for 24 h. To induce chemical LTP (cLTP), neurons were cultured for 20 min at 37 °C in 5% CO_2 and in a bath solution containing 200 µM glycine (in mM: 129 NaCl, 4 KCl, 4 $CaCl_2$, 10 HEPES, and 10 glucose [pH 7.4]). As a control (Vehicle), the cells were incubated in a glycine-free bath solution containing 4 mM $MgCl_2$. The neurons were immediately put on ice and rinsed once with ice-cold PBS before they were lysed by scraping in lysis buffer (10 mM HEPES pH 7.4, 150 mM NaCl, 10 mM EDTA, 1% Triton X-100, Roche protease inhibitor cocktail tablets "Complete mini EDTA-free", and Roche phosphatase inhibitor cocktail tablets "PhosStop"). The lysates were centrifuged at 500 × *g* for 5 min at 4 °C and diluted with 4× sample loading buffer (300 mM Tris-HCl pH 6.8, 12% (w/v) SDS, 0.6% (w/v) bromophenol blue, 60% (v/v) glycerol, and 600 mM β-mercaptoethanol) before boiling. The levels of pGluA1 total-GluA1 and PTEN samples were compared in western blots of Tris-glycine SDS gels.

Electrophysiology

Acute Slice Preparation

Mice were anesthetized with an intraperitoneal injection of Thiobarbital (346836, Braun), perfused transcardially (only when used for patch-clamp recordings) with cold choline ACSF at pH 7.35 (92 mM choline Cl, 2.5 mM KCl, 1.25 mM NaH_2PO_4, 30 mM $NaHCO_3$, 20 mM HEPES, 20 mM glucose, 2 mM thiourea, 5 mM Na-ascorbate, 3 mM Na-pyruvate, 0.5 mM $CaCl_2$, and 3 mM $MgSO_4$), and then decapitated. Coronal slices (300 µm) containing the amygdala were prepared in the same solution and maintained for 10 min in that solution at 32 °C. The slices were then moved to a recovery chamber for 1 h at 25 °C in HEPES holding ACSF at pH 7.35 (92 mM NaCl, 2.5 mM KCl, 1.25 mM NaH_2PO_4, 30 mM $NaHCO_3$, 20 mM HEPES, 25 mM glucose, 2 mM thiourea, 5 mM Na-ascorbate, 3 mM Na-pyruvate, 2 mM $CaCl_2$, and 2 mM $MgSO_4$), before transferring them into a submersion-type recording chamber perfused with ACSF and saturated with 5% CO_2/95% O_2 at 25 °C in the electrophysiology set-up.

Field Recording

A concentric bipolar platinum-iridium stimulation electrode was placed on the fibers arising from the auditory cortex or the thalamus (TL), and a low-resistance glass recording microelectrode filled with ACSF (3–4 MΩ resistance) was situated in the LA or the CA1 to record the field excitatory postsynaptic potentials (fEPSPs). An input–output curve was recorded for each slice to compare the basal synaptic transmission under different conditions. This curve was also used to set the baseline fEPSP of the maximal slope for the long-term depression (LTD) and long-term potentiation (LTP) experiments. Baseline stimulation was delivered every 15 s (0.01 ms pulses) for at least 20 min before LTD or LTP induction to ensure the stability of the response. LTD was induced using 900 pulses at 1 Hz and responses were recorded for 1 h after inducing the LTD. LTP in the LA was induced by high-frequency stimulation (100 Hz, 1 s, 4 trains) and by theta-burst stimulation in the CA1, and the responses were recorded for 1 h after induction. To monitor the paired-pulse ratio (PPR) at auditory cortex-lateral amygdala (AC-LA), thalamus-lateral amygdala (TL-LA), and CA1 (stratum radiatum) synapses, we stimulated the axons with 2 pulses separated by increasing interstimuli intervals (10, 20, 30, 40, 50, 100, 200, and 400 ms).

Behavioral Assays

Animals were handled for 5 min in the experimental room on each of the 3 days before beginning the experiments. Experimental mice were transferred to the behavioral testing room 30 min prior to beginning the first trial in order to habituate them to the room. To avoid the influence of circadian fluctuations, the behavioral tests were performed during the light period, from 09:00 to 15:00 h. All behavioral parameters were scored from videos by investigators who were blind to the genotype.

Fear Conditioning

In this test, the mice form an association between a context (an experimental cage/tone) and an aversive event (a footshock) that takes place in association with that context. When placed back into the context, mice exhibit a range of conditioned fear responses, including immobility (freezing). Training and testing took place in a rodent observation cage (30 × 37 × 25 cm) placed in a sound-attenuating chamber. In the training (conditioning) session, the mouse was exposed to the conditioning context (180 s) followed by a tone (CS 20 s, 2 kHz, 85 dB). After termination of the tone, a foot shock (US 0.75 mA, 2 s) was delivered through a stainless steel grid floor. Mice received 3 footshocks with an intertrial interval of 60 s. The mouse was removed from the fear-conditioning box 30 s after shock termination and returned to their home cages. *Testing*. In contextual fear conditioning, mice were placed back into the original training context for 8 min, during which no footshock was delivered. For auditory-cued fear-conditioning, animals were placed into a novel context (same cages but with different walls, floor, and background odor), and after a 3 min baseline period they were re-exposed to the tone for 5 min (same characteristics as at conditioning), yet in the absence of footshocks. The animals' behavior was scored by an observer blind to the treatment conditions. Using a time-sampling procedure every 2 s, each mouse was scored blindly as either freezing or active at the instant the time-sample was taken. Freezing was defined as behavioral immobility except for movement needed for respiration.

Pain Threshold

One day after the cued fear-conditioning test, each mouse was placed individually in the conditioning chamber. After 120 s, the electric current was gradually increased at a rate of 0.05 mA/20 s until the animal showed the first signs of discomfort (moving backwards and flicking their hind legs) or pain (jumping and

vocalization). At this moment, the current was immediately switched off and the corresponding current was recorded as a measure of the animal's discomfort/pain threshold. Experiments were recorded using the Any-Maze Video Tracking System version 4.82 (Stoelting Co) with a camera fixed in front of the apparatus and connected to a computer.

Barnes Maze

The Barnes circular maze (Barnes 1979) was employed to assess spatial reference memory by training an animal to locate a hidden escape tunnel located directly beneath one of the holes at the perimeter of a large circular platform, which was brightly lit to provide a low-level aversive stimulus. Mice learn the location of the escape hole with the help of spatial reference points. This maze is an alternative to the Morris water maze because it is considered to be less anxiogenic given that it does not involve swimming. The Barnes maze consists of a flat, circular disk with 20 holes around its perimeter that permit the animal to exit the maze into an escape box. Only one hole is open (the escape hole), which has a cage underneath with clean bedding (the escape box). The maze was divided into 4 quadrants of equal size, placing the escape hole in the middle of one of the quadrants equidistant from the sidewalls. The testing room contained numerous maze cues. The behavior of the animal was monitored with a video camera mounted on the ceiling above the center of the maze, computerized by a tracking system (Ethovision Noldus IT). The Barnes maze task was performed in 2 successive phases. The acquisition phase was divided into 4 training sessions (days 1–4) and 1 probe session (day 5). Each training session includes 4 trials of 5 min each with 30 s intertrial intervals between trials 1–2 and 3–4 and a 30 minute intertrial interval between trials 2–3. The starting point was the middle of the maze, where the animals were placed for 30 s before each trial. A training session ended when the mouse entered the escape hole or when 5 min had elapsed, whichever came first. If the mouse did not find the escape hole within the 5 min of the trial, the experimenter gently guided the animal to the escape hole. In this case, the escape latency was recorded as 300 s and the mouse was then allowed to remain in the cage for 30 s. A 60 s probe session (day 5) was performed 24 h after the last trial of the learning period, during which the escape hole was closed. The parameters analyzed were the latency to find the escape hole and the number of holes searched by each mouse before finding the escape hole (number of errors).

Reversal Barnes Maze

This reversal task evaluates the ability to change a routine behavior or something previously learned, and it depends on the orbitofrontal cortex. A day after the memory test, the location of the escape hole is changed to a different quadrant of the maze. The ability of the subjects to find the new location is evaluated as described previously and quantified by the number of retraining sessions required to consistently choose the new hole.

Novel Object Location

This assay was chosen because it is not intrinsically stressful, a factor that crucially affects the cognitive performance of mice in other spatial learning paradigms (e.g. the Morris water maze). The memory tests consisted of 3 phases—"habituation", "sample", and "choice" trials. Mice were first individually habituated for 30 min to an empty open field box ($35 \times 35 \times 15$ high cm). The sample trial (object exposure) consisted of placing the mouse into the test box that contained 2 identical objects. The mouse was removed from the test box and after a 30 min delay (retention period), the mouse was placed back into the test box for a choice trial. A choice trial consisted of switching the location of one of the objects (Novel Object Location trial) and a recognition index was calculated by dividing the total time spent exploring the displaced object by the total time spent exploring both objects during the test session. A recognition index of 0.5 would therefore correspond to equal exploration of both objects. Subjects were excluded from the analysis if they failed to explore both objects for a total of at least 10 s during either training or test sessions. One mouse was excluded from this study based on this criterion.

Three-Chamber Social Recognition Test

This task is typically used to quantify the social behavior of mice, measuring their tendency to approach another mouse and engage in social investigation (Crawley 2004). The mice are allowed olfactory and minimal tactile interaction with a possible social or inanimate target. The social testing arena is a rectangular, 3-chambered apparatus, with dividing walls made of clear methacrylate and openings that give access to each chamber. An unfamiliar mouse that had had no prior contact with the mouse being tested is situated in one of the chambers (social target). This animal was always of the same background, age, and gender as the experimental mouse, and it was enclosed in a wire cage that allowed visual, olfactory, auditory, and some tactile contact, but that prevented fighting. These target animals had previously been habituated to the small wire cage for 10 min on each of 3 days. An identical wire cage was placed in the opposite chamber containing a small black object (inanimate target) that serves as a control for the exploration of a novel object in a novel environment. The test mouse was placed in the middle chamber and allowed to explore this area for 5 minutes as a habituation period, enabling the mouse to recognize this chamber as a familiar "home base". Subsequently, the openings to the side chambers were revealed and the mouse was allowed to explore the entire social arena during a 10 min session. The amount of time spent in each chamber and the number of entries into each chamber, as well as the time and number of visits to each target, were recorded using a video-tracking system and analyzed with the Any-Maze software. To determine whether the data truly reflect actual exploration of the social target, a human observer recorded the time that the subject spent directly exploring the wire cage containing the strange mouse or the nonsocial target. The chambers and the wire cages were cleaned with 0.1% acetic acid between trials.

EPM

The elevated plus maze (EPM) is used to measure anxiety-like behavior in laboratory animals. The test is based on the natural aversion of mice for open and elevated areas, as well as on their natural spontaneous exploratory behavior in novel environments. Animals were placed in a maze made of methacrylate that consisted of a central quadrant (5×5 cm), with 4 arms (5×25 cm). Two of the arms had opaque walls (16 cm high) around the edge (closed arms), while the other 2 arms did not have walls (open arms). The maze was elevated 45 cm above the floor on a plus-shape plywood stand, and the animal was placed at the center of the maze, facing one of the enclosed arms. During a 5 min test period, the parameters measured were the

time spent in each arm and the total number of arm entries, both open and closed.

Open Field

The open field arena was constructed of a 40 × 40 cm laminated wood floor surrounded by clear, 30 cm high acrylic walls. A 4 × 4 grid matrix was painted on the floor of the open field, dividing the field into 16 squares (12 outer and 4 inner) each measuring 10 × 10 cm. At the beginning of the open field session, the mouse was placed on the right front corner square (relative to the position of the experimenter) and they were retained inside a clear acrylic tube. After 30 s, the tube was lifted out of the arena and the mouse was allowed to move freely about the open field for a period of 5 min before returning it to its home cage. The speed of the mouse and the distance traveled during the 5 min trial were measured. The open field was washed with 0.1% acetic acid between each session.

Self-Grooming

Self-grooming is considered a stereotyped or repetitive behavior when the sequence persists for unusual periods of time. Mice were scored for spontaneous grooming behavior as described earlier (Silverman et al. 2010). Each mouse was placed individually into a standard cage with a thin (1 cm) layer of bedding to reduce neophobia while preventing digging, a potentially competing behavior. The cumulative time each mouse spent grooming any body region was scored over 10 min. The cage and wood-chip bedding was changed between animals.

USV

Isolation-induced ultrasonic vocalization (USV) is used to measure the USVs emitted by pups when separated from their mother and littermates. Pups were isolated from the mother for 15 min while controlling their body temperature with infrared light and an electric blanket. The pups were removed from the nest individually, and randomly and gently placed into an isolation container: a plastic dish 100 × 20 mm. USV emission was monitored with an UltraSoundGate Condenser Microphone CM 16/CMPA (Avisoft Bioacoustics), and the microphone was connected via an UltraSoundGate 16Hb audio device (Avisoft Bioacoustics) to a computer, where the acoustic data were recorded with a sampling rate up to 300 000 Hz in 16-bit format using an Avisoft RECORDER (version 4.2.21, Avisoft Bioacoustics). The microphone used for recording was sensitive to frequencies of 20–135 kHz with a flat frequency response (3 dB). The accuracy of call detection by the software was verified manually by an experienced user. Prior to each test and between animals, the behavioral equipment was cleaned with a 70% ethanol solution and dried with paper towels.

Western Blotting

Unless indicated otherwise, tissues were homogenized in a buffer composed of 10 mM HEPES, 150 mM NaCl, 10 mM EDTA, and 1% Triton X-100 (pH 7.4). Protease Inhibitor Cocktail Tablets "Complete mini" (1:7) and Phosphatase Inhibitor Cocktail Tablets "PhosStop" (1:10) were prepared following the manufacturer's (Roche) instructions. The same quantity of protein was diluted in 6× sample loading buffer (300 mM Tris-HCl [pH 6.8], 12% (w/v) SDS, 0.6% (w/v) bromophenol blue, 60% (v/v) glycerol, and 600 mM β-mercaptoethanol). Samples were boiled at 95 °C for 5 min and subjected to 8% SDS-PAGE. The proteins were transferred to PVDF membranes (pore size, 0.45 µm; Cat. IPVH00010 Immobilon), which were blocked for 1 h in 0.1% Tween-20 in Tris-NaCl buffer (TBS-T) containing 5% nonfat milk powder. The membranes were probed overnight at 4 °C with the primary antibodies in the same blocking buffer and after washing with blocking buffer, the membranes were incubated for 1 h at room temperature with a secondary antibody coupled to horseradish peroxidase. After 3 washes with TBS-T, the corresponding proteins were visualized by enhanced chemiluminescence (Immobilon™ Western Chemiluminescent HRP Substrate; Millipore).

Statistical Analysis

Statistical tests were carried out using GraphPad Prism version 7.00 for Windows (GraphPad Software; www.graphpad.com). Unless otherwise indicated, the statistical differences were calculated using a nonparametric 2-tailed test (Mann–Whitney test) or with 2-way analysis of variance (ANOVA). For the cumulative frequency analysis, *P* values were determined with the Kolmogorov–Smirnov test. The details of the statistical test employed for each experiment appear in the figure legends.

Results

Mice Overexpressing PTEN Exhibit Microcephaly and Reduced Neuronal Growth

To evaluate the consequences of PTEN overexpression, we first analyzed the global features of the brain of Pten^{tg} mice. We used unbiased stereology to determine the brain size in WT and their Pten^{tg} littermates. As might be expected from the role of PTEN in limiting cell growth and proliferation (Stiles et al. 2004), Pten^{tg} mice developed significant microcephaly with a 29% decrease in forebrain volume (Fig. 1*a*). This decrease in brain size was proportional to the lower body weight of Pten^{tg} mice (Ortega-Molina et al. 2012). Size reduction of LA plus basolateral amygdala (LA + BLA) was not statistically significant in Pten^{tg} mice, as compared to their WT littermates (Fig. 1*b*). We then determined the structural connectivity in Pten^{tg} mice by quantifying the excitatory synaptic density in the LA by electron microscopy. We detected a significantly reduced synaptic density in Pten^{tg} mice (Fig. 1*c*,*d*). There was also a small reduction in the size of the PSD, with fewer synapses having large PSDs in Pten^{tg} mice (see the leftward shift in the cumulative frequency plot of PSD length; Fig. 1*e*). At the cellular level, the total surface area was also lower in Pten^{tg} neurons, as assessed by whole-cell membrane capacitance of LA pyramidal-like neurons (Fig. 1*f*).

We then assessed morphological properties of LA pyramidal-like neurons. We traced the morphology of neurons after whole-cell biocytin filling (see representative examples in Fig. 1*g*). As shown in Figure 1*h*,*i*, we found that PTEN overexpression produced a substantial reduction in dendritic complexity (Sholl analysis). Spine density was also diminished in neurons from Pten^{tg} animals, particularly on distal dendrites (Fig. 1*j*–*l*). Thus, an excess of PTEN restricts neuronal growth, leading to a substantial decrease in dendritic branching and synapse number.

As a reference, we also examined morphological properties of hippocampal pyramidal neurons in Pten^{tg} mice (Supplementary Fig. 1). Essentially, we observed similar trends for growth reduction as described for the LA. In this case, total hippocampal volume was significantly reduced in Pten^{tg} mice (Supplementary Fig. 1*b*), as well as spine and synaptic densities (Supplementary Fig. 1*c*–*e*), although there was no change in PSD length (Supplementary Fig. 1*f*).

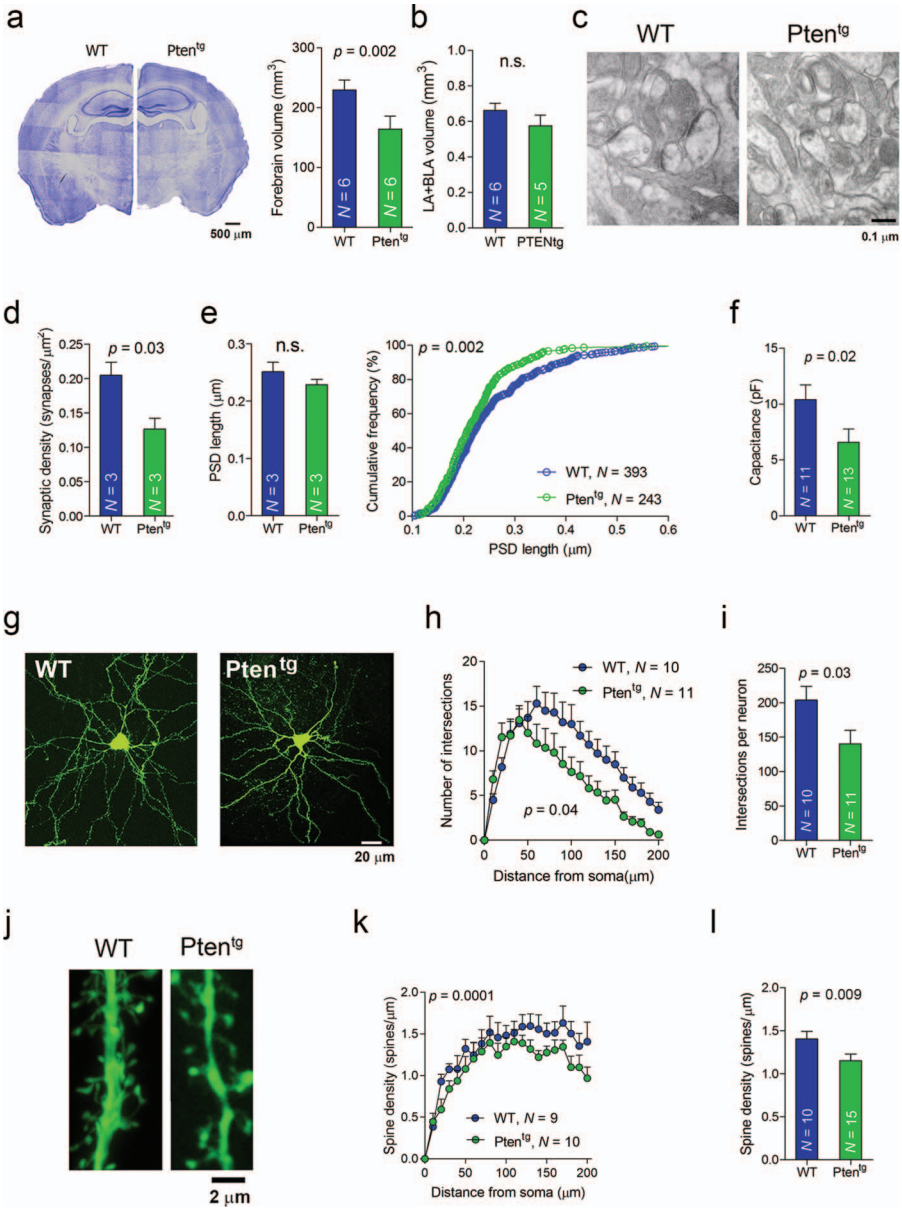

Figure 1. Microcephaly and weaker structural connectivity in the LA on Pten^{tg} mice. (*a*) Left, Nissl-stained coronal sections of the hemispheres from WT and Pten^{tg} mice obtained with a 40× objective and tile scanned. Right, bar graph showing the forebrain volume, where *N* represents the number of mice and the *P* value was determined with a 2-tailed Mann–Whitney test ($F = 1.780$, DFn = 5, DFd = 5). (*b*) The volume of the LA + BLA was determined by unbiased stereology on Nissl-stained preparations, determining the *P* value with a 2-tailed Mann–Whitney test ($P = 0.58$, $F = 2.216$, DFn = 5, Dfd = 5). (*c*) Representative electron micrographs from WT and Pten^{tg} mice depicting the LA neuropil, including the presynaptic and postsynaptic compartments. (*d*) Quantification of synaptic density, where *N* represents the number of mice. The total number of synapses analyzed was 393 for WT and 243 for Pten^{tg} mice. *P* value was determined with unpaired 2-tailed *t*-test ($t = 3.173$; df = 4). (*e*) Left, the length of the PSD in LA synapses, where *N* represents the number of mice and the *P* value was determined with an unpaired 2-tailed *t*-test ($P = 0.45$, $t = 0.807$; df = 4). Right, cumulative frequency of the PSD lengths, where *N* represents the number of synapses and the *P* value was determined with a Kolmogorov–Smirnov test (Kolmogorov–Smirnov $D = 0.1482$). (*f*) The membrane capacitance of LA neurons was determined during patch-clamp recordings, with *N* representing the number of cells and the *P* value determined with a 2-tailed Mann–Whitney test ($F = 1.053$, DFn = 10, Dfd = 12). (*g*) Projection confocal images (×40, tile scan) of pyramidal-like neurons in the LA that were filled with biocytin during patch-clamp recording and processed with Streptavidin-Alexa488. (*h*) The number of dendritic intersections is shown as a function of the distance from the soma (Sholl analysis), the parameters determined with Neurolucida software by tracing the dendritic tree in confocal stacks. A 2-way ANOVA revealed a significant ($P = 0.002$) 2-way interaction for the number of intersections (distance from soma by genotype, $F = 2.23$; DFn = 20; DFd = 380). The effect of the genotype was significant ($P = 0.04$, $F = 4.74$, DFn = 1, DFd = 19). (*i*) The total number of dendritic intersections, with *N* representing the number of cells and the *P* value determined with a 2-tailed Mann–Whitney test ($F = 1.051$, DFn = 10, Dfd = 9). (*j*) Confocal projection images of representative dendrites (×63, following deconvolution) from LA neurons filled with biocytin during patch-clamp recording and processed with Streptavidin-Alexa 488. (*k*) Sholl analysis of the spine density as a function of the distance from the soma, with *N* representing the number of cells. A 2-way ANOVA revealed a nonsignificant ($P = 0.98$) 2-way interaction for spine density (distance from soma by genotype, $F = 0.43$, DFn = 20, DFd = 327). The effect of genotype was significant ($P = 0.0001$, $F = 23.25$, DFn = 1, DFd = 327). (l) The average spine density per neuron, where *N* represents the number of cells and the *P* value was determined with a 2-tailed Mann–Whitney test ($F = 1.090$, DFn = 14, Dfd = 9). The data in all the graphs are represented as the mean ± standard error of the mean (s.e.m.).

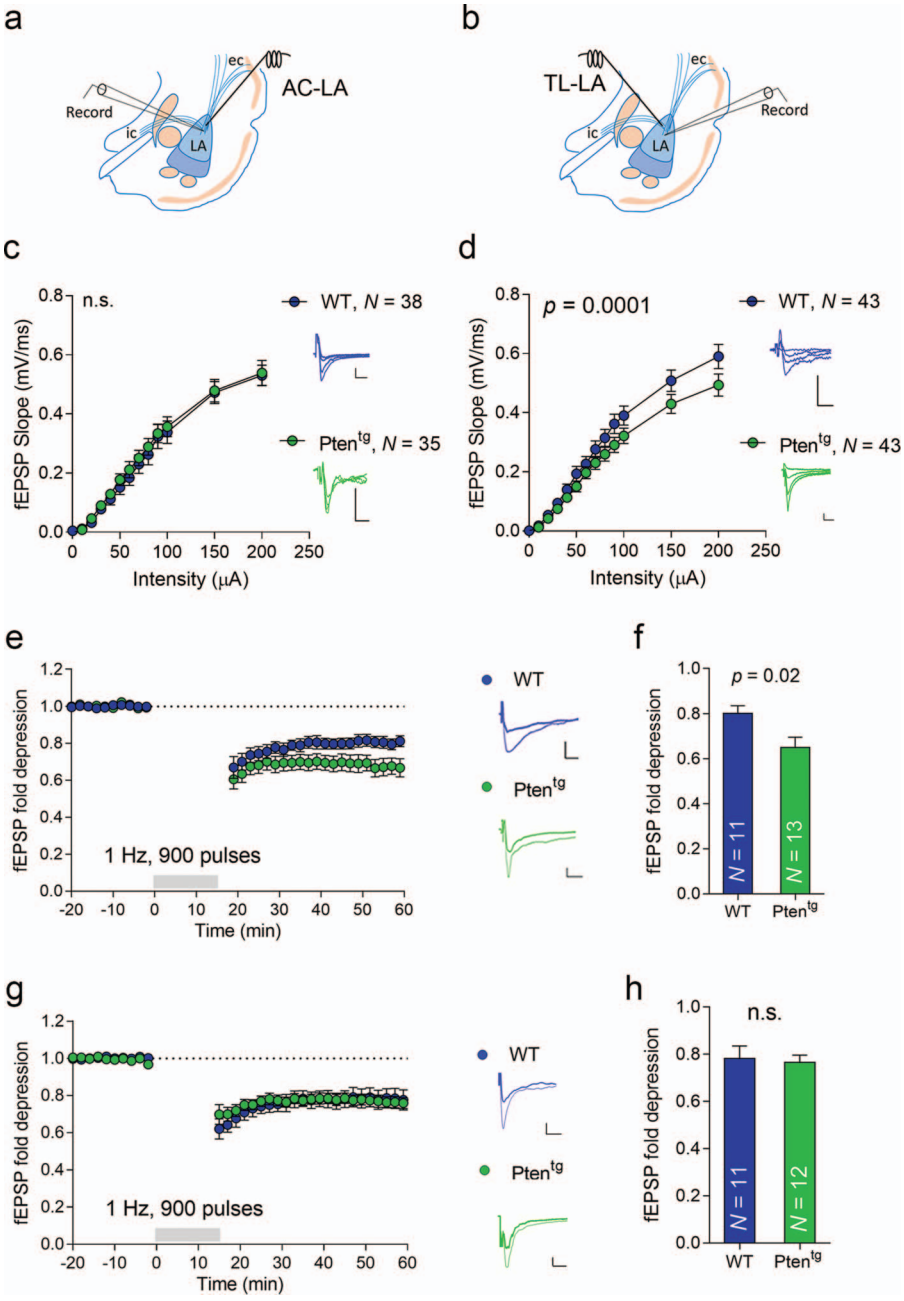

Figure 2. Basal synaptic transmission and LTD in LA synapses from Pten^{tg} mice. (*a* and *b*) Diagram of a coronal brain slice containing the amygdala. To stimulate the AC-LA pathway, an electrode was placed on the fibers arising from the external capsule ("ec", *a*), and to stimulate the TL-LA pathway, an electrode was placed in the internal capsule ("ic", *b*). fEPSPs were obtained in the LA. (*c* and *d*) Input–output curves of the fEPSPs evoked by stimulating axons arising in the auditory cortex (*c*) or thalamus (*d*) and recorded in the LA. Insets. Superimposed representative fEPSPs at 10, 50, 100, and 200 μA, determining the *P* values with a 2-way ANOVA. For *d*, a 2-way ANOVA revealed a nonsignificant ($P = 0.09$) 2-way interaction for the fEPSP slope (stimulation intensity by genotype, $F = 1.56$, DFn = 12, DFd = 654). The effect of the genotype was significant ($P < 0.0001$, $F = 27.01$, DFn = 1, DFd = 654), as was the effect of the stimulation intensity ($P < 0.0001$; $F = 45.57$, DFn = 12, DFd = 654). (*e* and *g*) Left, NMDAR-dependent LTD was induced in the LA in coronal slices taken from WT or Pten^{tg} mice (900 pulses at 1 Hz) stimulating axons arising from the auditory cortex (*e*) or thalamus (*g*). Right, representative fEPSPs before (thin line) and after (thick line) LTD induction: scale bars represent 0.5 mV, 20 ms. (*f* and *h*) Quantification of the average maximal fEPSP slopes 50–60 min after induction, relative to baseline response in the AC-LA (*f*) or TL-LA (*h*) synapses. *N* represents the number of slices and the *P* values were determined with a 2-tailed Mann–Whitney test ($F = 2.235$, DFn = 12, DFd = 10 for *f*; $P = 0.55$, $F = 2.749$, DFn = 9, DFd = 10 for *h*). The data in all the graphs are the mean ± s.e.m.

Excess PTEN Skews Synaptic Plasticity Toward Depression in Auditory Cortex-LA Synapses

We then evaluated whether the structural alterations in the Pten^{tg} mice are accompanied by functional changes in synaptic physiology. We first evaluated basal synaptic transmission by recordings of fEPSP in acute coronal slices from WT and Pten^{tg} mice containing the LA (Fig. 2*a*,*b*). To assess the function of excitatory synapses without the contribution of GABAergic inputs, all electrophysiological recordings were performed in the

presence of picrotoxin (100 µM), a noncompetitive antagonist of $GABA_A$ receptors. In slices from $Pten^{tg}$ mice, synapses receiving input from the auditory cortex (AC-LA pathway; Fig. 2*a*) exhibited normal basal transmission (input–output curves; Fig. 2*c*), whereas a small but significant decrease in basal transmission was observed at synapses receiving thalamic input (TL-LA pathway; Fig. 2*b*,*d*). To note, passive membrane properties of LA neurons, measured under whole-cell configuration (Supplementary Fig. 2*a*,*b*), were not affected in $Pten^{tg}$ mice.

Given the distinct role of PTEN in NMDAR-dependent LTD at hippocampal CA3-CA1 synapses (Wang et al. 2006; Jurado et al. 2010), we tested whether LTD was altered in LA circuits of $Pten^{tg}$ mice. We induced LTD at LA synapses in coronal slices by stimulating afferents from the AC or TL (15 min at 1 Hz) and recording the fEPSPs in the LA. Interestingly, LTD was enhanced in $Pten^{tg}$ mice at AC-LA synapses (Fig. 2*e*,*f*), but not at synapses in the TL-LA pathway (Fig. 2*g*,*h*). Incidentally, LTD at hippocampal CA3-CA1 synapses was also normal (Supplementary Fig. 2*c*,*d*). Therefore, these data suggest that PTEN overexpression enhances LTD expression at LA excitatory synapses, specifically those of the AC-LA circuit.

We then evaluated LTP, as another major form of synaptic plasticity underlying learning and memory in the LA (Rogan et al. 1997; Maren and Quirk 2004; Rumpel et al. 2005). In slices from $Pten^{tg}$ mice, there was significantly less LTP at synapses in the AC-LA pathway (Fig. 3*a*), whereas LTP at TL-LA synapses remained unaffected (Fig. 3*b*). As a reference, LTP at hippocampal CA3-CA1 synapses was also impaired (Supplementary Fig. 2*e*,*f*). These findings imply that excess PTEN impairs synaptic potentiation at specific neuronal circuits, in the case of the LA, at the AC input.

We have previously shown that PTEN is directly involved in the mechanism for LTD, whereas this does not appear to be the case for LTP (Arendt et al. 2010; Arendt et al. 2014). Nevertheless, PTEN may indirectly control the extent of LTP expression by antagonizing PI3K activity, which is required for LTP (Man et al. 2003; Opazo et al. 2003; Arendt et al. 2010). To determine whether excess PTEN can indeed impair LTP induction (and to bypass possible neurodevelopmental effects in $Pten^{tg}$ mice), we overexpressed EGFP-tagged PTEN (EGFP fused to the N-terminus of PTEN) for 48 h in primary hippocampal neurons using a viral vector (Jurado et al. 2010) (Fig. 3*c*; EGFP expression was used as a control for the potential effect of viral infection). Quantification of PTEN levels under these conditions showed a 2.6-fold increase in the total levels of PTEN (endogenous plus recombinant) in EGFP-PTEN-expressing cultures, with respect to EGFP expression (Fig. 3*d*,*e*). We then induced LTP using a well-established chemical protocol (cLTP) with 200 µM glycine (Lu et al. 2001; Passafaro et al. 2001) to maximize the number of synapses undergoing plasticity. As shown in Figure 3*f*,*i*,*j* (two left-most columns), cLTP produced a marked increase in calcium/calmodulin-dependent protein kinase II (CaMKII) phosphorylation at Thr286, as well as on its substrate, GluA1-Ser831, in EGFP-expressing neurons. These 2 phosphorylation events are associated to LTP induction (Barria et al. 1997; Mammen et al. 1997; Lisman et al. 2012). In contrast, the increase in GluA1 and CaMKII phosphorylation after cLTP induction was abolished in neurons overexpressing PTEN (Fig. 3*f*,*i*,*j*; two right-most columns), suggesting that PTEN overload quenches intracellular signaling leading to LTP. To note, total levels of GluA1 and CaMKII were not affected by PTEN overexpression, suggesting that synaptic stability or general neuronal health is not compromised for the duration of this experiment (Fig. 3*f*–*h*).

Amygdala Activation and Fear Memory Retrieval Are Compromised by PTEN Overexpression

To evaluate whether these differences in neuronal structure and synaptic function would correlate with specific brain region activation, we carried out PET coupled to computerized tomography imaging (micro-CT). First of all, in accordance with the results of unbiased stereology (Fig. 1*a*), micro-CT identified a significant decrease in the dimensions of the head of $Pten^{tg}$ mice (intracranial volume; Fig. 4*a*). To determine if this decrease in brain and head size was accompanied by changes in basal brain activity, we scanned the mice by micro-CT-PET using a radiolabeled glucose analogue (2-deoxy-2-[18F]fluoro-D-glucose, ^{18}F-FDG) as the tracer (Magistretti and Pellerin 1999). We identified significantly less activity in the frontal and auditory cortices, and in the ventral hippocampus of $Pten^{tg}$ mice, as compared to WT littermates (Fig. 4*b*,*c*; Supplementary Fig. 3*a*). Notably, the changes in basal activity were region specific as they were not detected in subcortical areas like the thalamus, and glucose uptake was even enhanced in the dorsal hippocampus of $Pten^{tg}$ mice. Thus, $Pten^{tg}$ mice present lower levels of basal cortical activity.

We then tested whether these differences in brain region activation affected cognitive performance. To this end, we combined PET imaging with an associative learning paradigm, namely auditory fear conditioning. In this form of Pavlovian learning, an aversive stimulus (an electrical footshock) is associated with a neutral stimulus (a tone), resulting in the expression of fear responses (freezing) to the originally neutral stimulus (Kim and Jung 2006). We trained mice repeatedly with mild electrical footshocks, delivered immediately after each auditory cue, and the brains of the mice were micro-CT-PET scanned immediately after conditioning (Fig. 4*d*; day 1) and again after retrieval (Fig. 4*d*; day 2). Compared to WT mice, $Pten^{tg}$ displayed overall less activity induced by fear conditioning (after subtraction of basal activity), although this difference was only significant in the auditory cortex (Supplementary Figs 3*b* and 4*a*). Importantly, both genotypes were equally sensitive to electrical shock (Supplementary Fig. 4*b*) and showed similar freezing behavior during the habituation period (Supplementary Fig. 4*c*).

We then elicited the retrieval of the fear response 24 h later by exposing the mice in a novel environment and presenting the auditory cue (tone). PET activity was analyzed again immediately after memory retrieval to define the activated brain areas and the potential effect of PTEN overexpression in $Pten^{tg}$ mice. During retrieval, glucose uptake was enhanced in areas known to be involved in auditory fear conditioning in WT mice, such as the hippocampus, amygdala, and thalamus (Kim and Jung 2006; Hunsaker and Kesner 2008; Fanselow and Dong 2010) (Fig. 4*e*,*f*; Supplementary Fig. 3*c*). Strikingly, this pattern of brain region activation was virtually reversed in $Pten^{tg}$ mice, as the activity in these same areas decreased (relative to their already reduced basal levels) following the tone (Fig. 4*f*; Supplementary Fig. 3*c*). These experiments suggest that excess PTEN significantly dampens activation in key brain areas during memory retrieval.

Interestingly, these results correlated very well with memory performance. Notably, freezing rates were considerably lower in $Pten^{tg}$ mice on presentation of the tone (Fig. 4*g*), implying impaired amygdala-dependent fear recall. Therefore, attenuation of thalamic and cortico-amygdala activation by PTEN overexpression is accompanied by a strong reduction in fear memory retrieval.

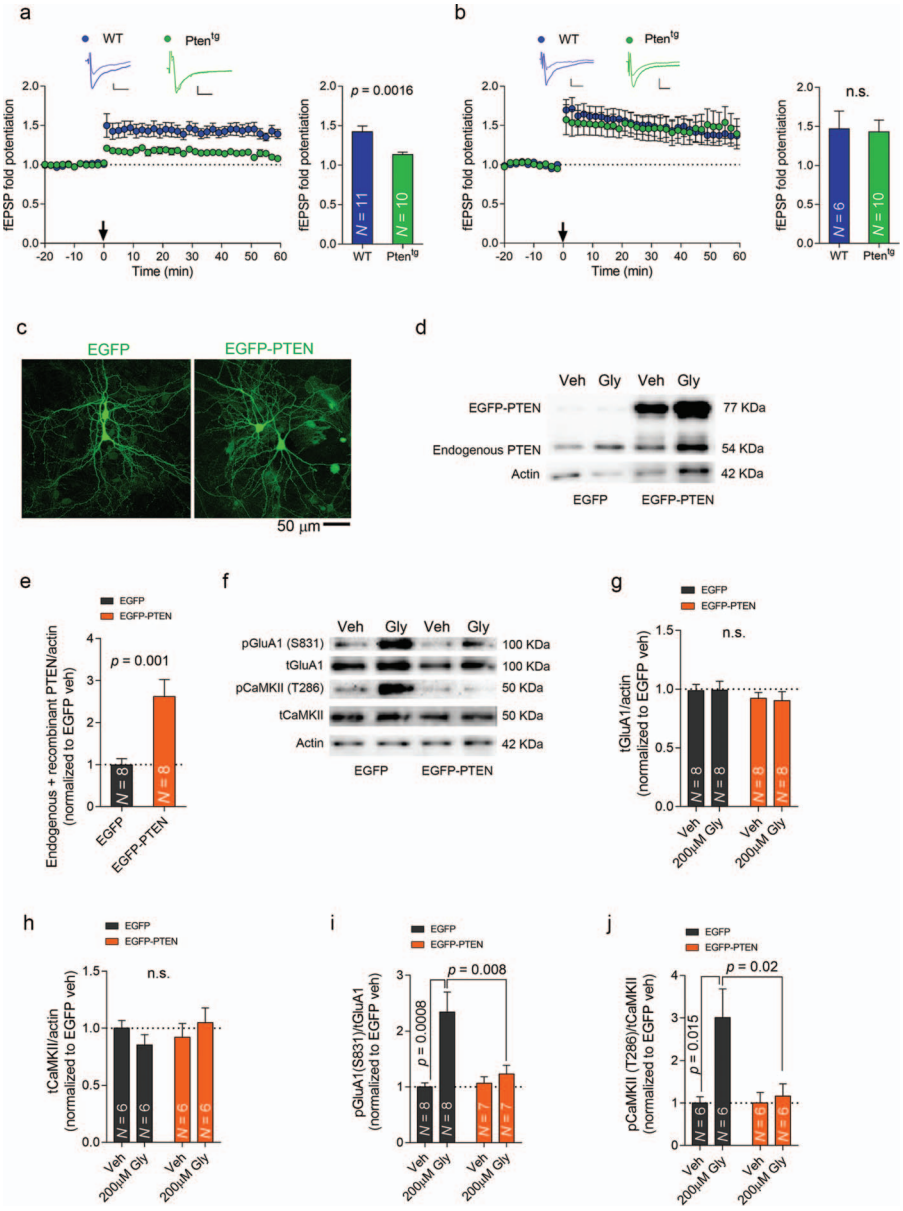

Figure 3. Impaired LTP and quenched LTP signaling in Pten^{tg} mice. (*a* and *b*) Left, LTP was induced in the LA in coronal slices (at 100 Hz frequency), stimulating axons arising from the auditory cortex (*a*) or the thalamus (*b*). Inset, representative fEPSPs before (thin line) and after (thick line) LTP induction: scale bars represent 0.5 mV, 20 ms. Right, quantification of the average maximal fEPSP slopes 50–60 min after induction, relative to baseline response in the AC-LA (*a*) and the TL-LA (*b*) synapses. *N* represents the number of slices, and the *P* values were determined with a 2-tailed Mann–Whitney test ($F = 5.578$, $DFn = 8$, $Dfd = 9$ for *a* and $P = 0.9$, $F = 3.814$, $DFn = 9$, $Dfd = 5$ for *b*). (*c*) Confocal projection images (×20) of primary hippocampal neurons expressing EGFP (left) or EGFP-PTEN (right). (*d*) Western blot of the homogenates from neurons infected with EGFP and EGFP-PTEN viral vectors and treated with 200 µM glycine or with the vehicle (Veh), showing endogenous PTEN and EGFP-PTEN (recombinant PTEN). (e) Quantification of total PTEN levels in cultures infected with EGFP-PTEN and EGFP viral vectors. *P* value was determined with a 2-tailed Mann–Whitney test ($F = 7.531$, $DFn = 7$, $Dfd = 7$) and *N* represents the number of cultures. (f) Western blot of the homogenates from neurons infected with EGFP and EGFP-PTEN viral vectors and treated with 200 µM glycine or with the vehicle, showing phospho-GluA1 at S831, total GluA1, phospho-CaMKII at T286, and total CaMKII. Actin is used as a loading control. (*g*) Total GluA1 levels in cultures treated with 200 µM glycine to induce cLTP. A 2-way ANOVA revealed a nonsignificant ($P = 0.85$) 2-way interaction for the tGluA1 levels (treatment by virus $F = 0.04$, $DFn = 1$, $DFd = 28$). The effect of the virus was not significant ($P = 0.25$, $F = 1.37$, $DFn = 1$, $DFd = 28$), neither was the effect of the treatment ($P = 0.90$, $F = 0.01$, $DFn = 1$, $DFd = 28$). (*h*) Quantification of total CaMKII after cLTP induction. A 2-way ANOVA revealed a nonsignificant ($P = 0.92$) 2-way interaction for the tCaMKII levels (treatment by virus $F = 1.70$, $DFn = 1$, $DFd = 20$). The effect of the virus was not significant ($P = 0.58$, $F = 0.32$, $DFn = 1$, $DFd = 20$), neither was the effect of the treatment ($P = 0.92$, $F = 0.01$, $DFn = 1$, $DFd = 20$). *N* represents the number of cultures. (i) Phospho-GluA1 levels in cultures treated with 200 µM glycine to induce cLTP. A 2-way ANOVA revealed a significant ($P = 0.012$) 2-way interaction for the pGluA1 levels (treatment by virus $F = 7.24$, $DFn = 1$, $DFd = 26$). The effect of the virus was significant ($P = 0.02$, $F = 5.71$, $DFn = 1$, $DFd = 26$), as was the effect of the treatment ($P = 0.002$, $F = 11.93$, $DFn = 1$, $DFd = 26$). The *P* values in the graph were determined by Sidak's multiple comparisons test. (*j*) Phospho-CaMKII levels in cultures treated with 200 µM glycine to induce cLTP. A 2-way ANOVA revealed a significant ($P = 0.03$) 2-way interaction for the pCaMKII levels (treatment by virus $F = 5.44$, $DFn = 1$, $DFd = 20$). The effect of the virus was significant ($P = 0.03$, $F = 5.44$, $DFn = 1$, $DFd = 20$), as was the effect of the treatment ($P = 0.01$, $F = 7.48$, $DFn = 1$, $DFd = 20$). The *P* values in the graph were determined by Sidak's multiple comparisons test. *N* represents the number of cultures. Data in all graphs are the mean ± s.e.m.

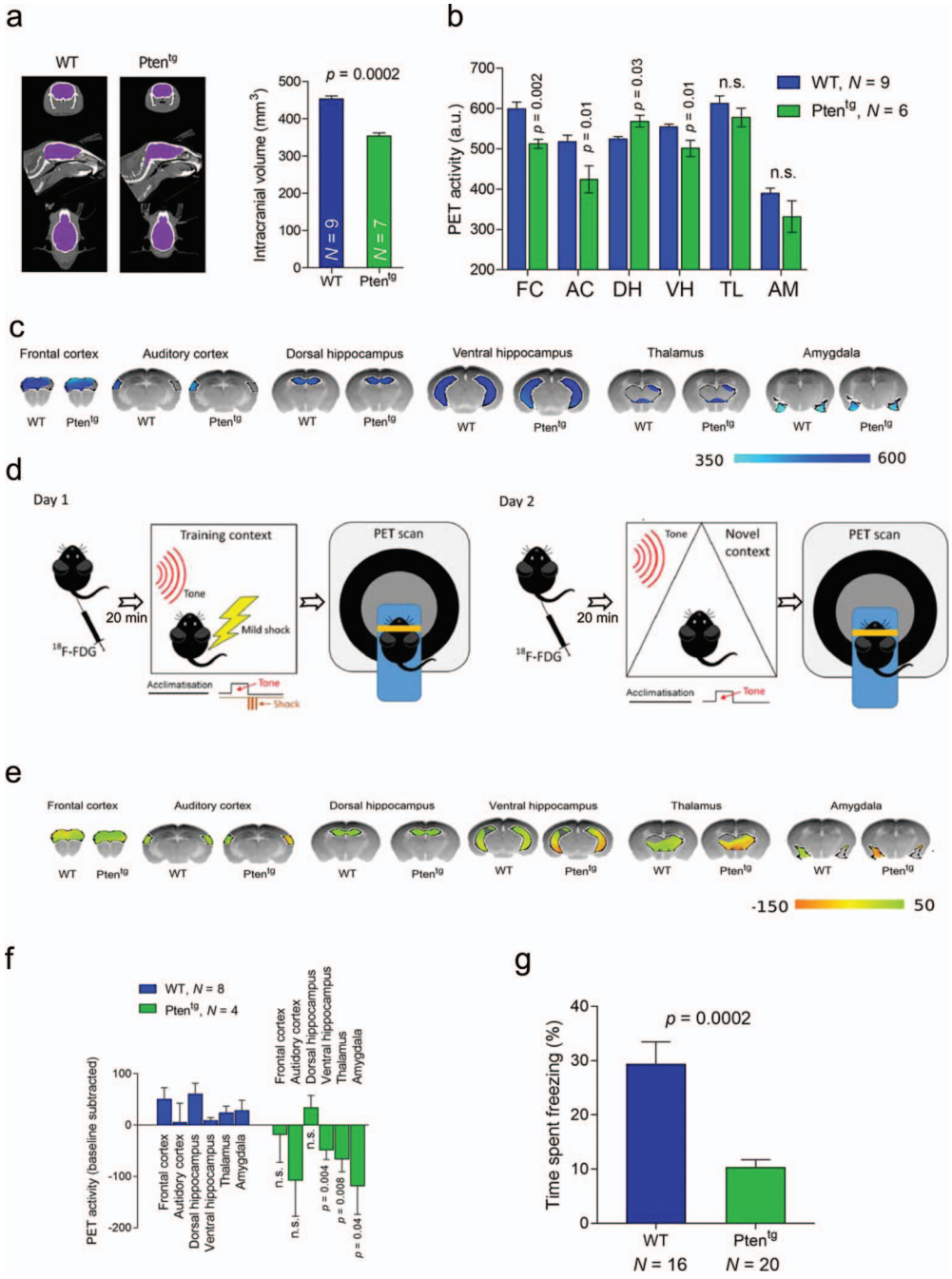

Figure 4. Impaired auditory fear conditioning and failed amygdala activation during retrieval in Pten^{tg} mice. (*a*) Left, representative micro-CT images of the cranium of WT and Pten^{tg} mice. Right, bar graph representing the average intracranial volume of WT and Pten^{tg} mice measured in the micro-CT images, where *N* represents the number of mice and the *P* value was determined with a 2-tailed Mann–Whitney test ($F = 1.013$, $DFn = 8$, $DFd = 6$). (*b*) Bar graphs representing the basal PET activity in selected brain areas. All *P* values were determined with a 2-tailed Mann–Whitney test, *N* representing the number of mice: $F = 3.164$, $DFn = 5$, $DFd = 8$ for the frontal cortex; $F = 3.061$, $DFn = 5$, $DFd = 8$ for the auditory cortex; $F = 3.479$, $DFn = 5$, $DFd = 8$ for the dorsal hippocampus; $F = 5.264$, $DFn = 5$, $DFd = 8$ for the ventral hippocampus; $F = 1.012$, $DFn = 5$, $DFd = 8$ for the thalamus; $F = 6.486$, $DFn = 5$, $DFd = 8$ for the amygdala. (*c*) Representative coronal images of PET activity in the regions quantified in *b*. The bar represents the color code for the crude PET values (the sagittal and horizontal planes are presented in the Supplementary Fig. 3*a*). (*d*) Design of the combined auditory fear conditioning and PET experiment. (*e*) Representative images of PET activity relative to the baseline values. The bar represents the color code for the relative PET values (the sagittal and horizontal planes are presented in Supplementary Fig. 3*c*). (*f*) PET activity immediately after retrieval of the auditory fear memory in WT and Pten^{tg} mice after baseline subtraction. All *P* values were determined with a 2-tailed Mann–Whitney test, with *N* representing the number of mice: $F = 2.801$, $DFn = 3$, $DFd = 7$ for the frontal cortex; $F = 1.773$, $DFn = 3$, $DFd = 7$ for the auditory cortex; $F = 1.547$, $DFn = 3$, $DFd = 7$ for the dorsal hippocampus; $F = 5.597$, $DFn = 3$, $DFd = 7$ for the ventral hippocampus; $F = 1.903$, $DFn = 3$, $DFd = 7$ for the thalamus; $F = 3.854$, $DFn = 3$, $DFd = 7$ for the amygdala. (*g*) Freezing during retrieval of auditory fear memory in WT and Pten^{tg} mice. *P* value was determined with a Mann–Whitney test ($F = 6.85$, $DFn = 15$, $DFd = 19$), and *N* represents the number of mice. The data in all the graphs are the mean ± s.e.m.

Impaired hippocampal-dependent learning by PTEN overepxression

Given that amygdala-dependent memory is impaired in Pten^{tg} mice and that synaptic plasticity was altered in both amygdala and hippocampal circuits, we examined whether excess PTEN may have broader effects on cognitive function. Specifically, to test hippocampal function, we assessed spatial learning and memory retention using the Barnes maze. In this test, mice escaped from a brightly lit, exposed circular open platform to a small dark recessed chamber located under one of the 20 holes around the perimeter of the platform (the escape hole). The Pten^{tg} mice made more errors in finding the escape hole during the learning phase (4 days, 4 trials per day; Fig. 5*a*). Accordingly, Pten^{tg} mice had a higher latency in reaching the escape hole (Fig. 5*b*). Nevertheless, these animals reached similar performance to their WT littermates by the last training day and displayed comparable reference memory in the probe trial (day 5, 24 h after the last training day; Fig. 5*c*,*d*).

Reversal training was conducted in the same manner as acquisition training, except that the escape hole was moved to the opposite side of the maze. Mice completed 2 days of reversal training with 4 trials per day. On the first day of reversal training, the Pten^{tg} mice made more errors (Fig. 5*e*) and required more time to reach the new escape hole (Fig. 5*f*). However, on the second day of the test, they had reached the same level of performance as WT mice (Fig. 5*e*,*f*).

The hippocampal-dependent memory of Pten^{tg} mice was further tested in the novel object location task. This task involves exposing the mice to 2 objects and then testing the animals after a 30-min delay, with one object moved to a novel location. Mice that remembered the original training experience preferentially explored the displaced object rather than the nondisplaced object. This preference (recognition index) was similar in both genotypes (Fig. 5*g*).

Altogether, these data suggest that while Pten^{tg} mice display a delay in hippocampal-dependent learning, they seem to reach a relatively normal hippocampal-dependent memory.

Pten Overexpression Intensifies Social Behavior and Reduces Anxiety

As mentioned earlier, PTEN overexpression constitutes the opposite genetic manipulation to PTEN deficiency, which is associated to some forms of autism spectrum disorder (PTEN-ASD) (Frazier et al. 2015; Yeung et al. 2017). In order to assess the instructive role of PTEN in this pathology, we tested autistic-related behaviors in Pten^{tg} mice. We first used the 3-chamber test for social interaction. In this assay, the mouse can move freely among 3 chambers, starting from the central chamber, with a strange mouse (social target) in one of the side chambers and an inanimate object in the opposite chamber. While both WT and Pten^{tg} mice exhibited a clear preference for the social target over the inanimate object (Fig. 5*h*), the latter spent significantly more time than their WT littermates interacting with the social target (Fig. 5*h*; two right-most columns), implying more intense social behavior.

As ASD patients tend to exhibit more anxiety (White et al. 2009), Pten^{tg} mice were tested in the EPM. These Pten^{tg} mice spent relatively longer times in the open arms of the EPM than their WT littermates (Fig. 5*i*), indicative of less anxiety-like behavior. Nevertheless, these animals displayed normal exploratory behavior in the open field test (Supplementary Fig. 5*a*,*b*) and normal grooming behavior (Supplementary Fig. 5*c*–*e*). As another paradigm related to social behavior and anxiety, we evaluated USVs in Pten^{tg} and WT pups separated from their mothers on postnatal days 3–12. Although USVs have different communication values in rodents, maternal separation-induced USVs are considered mostly a stress or anxiety response from pups to elicit maternal care (Heckman et al. 2016). As shown in Figure 5*j*–*l*, Pten^{tg} pups produced fewer (panel j) and shorter calls (panel k), which were also of lower intensity (panel l). Other parameters like peak frequency were no different between the WT and Pten^{tg} mice (not shown). Therefore, the overall USV response to maternal separation was milder in Pten^{tg} pups, which may reflect lower levels of anxiety in these animals.

Together, these findings suggest that PTEN overexpression enhances some forms of social communication and reduces anxiety-related behavior, even over physiological values observed in WT mice.

Pten-ΔPDZ Mice Exhibit Slight Macrocephaly and Impaired LTD at AC-LA Synapses

Given the alterations in synaptic plasticity we have observed for Pten^{tg} mice, it is tempting to speculate that at least part of the behavioral phenotype observed in these animals is due to specific functions of PTEN at synapses. To approach this hypothesis, we analyzed the knock-in mouse in which PTEN lacks its C-terminal PDZ-binding motif (truncation of residues 399–403, Pten-ΔPDZ), therefore preventing PTEN interaction with the PDZ domains of PSD-95 (Jurado et al. 2010; Knafo et al. 2016). Importantly, this truncation does not alter PTEN expression or catalytic activity (Jurado et al. 2010; Knafo et al. 2016). However, we cannot rule out that other non-synaptic functions of PTEN may also be altered in these mice.

Pten-ΔPDZ mice had normal weight, as compared to WT littermates (Fig. 6*a*), consistent with overall normal growth in these animals. We then evaluated brain morphology and synaptic connectivity. Using unbiased stereology on Nissl-stained slices, we detected a small but significant macrocephaly in Pten-ΔPDZ mice (Fig. 6*b*), suggesting that PTEN PDZ interactions participate to some extent in developmental programs determining brain size. Similar to Pten^{tg} animals, the size of the LA plus the BLA was not significantly different to WT animals in Pten-ΔPDZ mice (Fig. 6*c*). To address structural connectivity, we examined the synaptic density and PSD length in the LA by electron microscopy. As shown in Figure 6*d*,*e*, these parameters were not significantly altered in Pten-ΔPDZ animals. These findings suggest that PTEN PDZ interactions are not critical for synaptogenesis nor do they define synaptic size in this region.

We then tested whether these synapses in Pten-ΔPDZ mice, with apparently normal structure, may have functional alterations. To this end, we measured NMDAR-dependent LTD at LA synapses. As shown in Figure 6*f*,*g*, LTD was virtually abolished at AC-LA synapses in Pten-ΔPDZ mice. Interestingly, and similar to the Pten^{tg} animals, the alteration in LTD was specific for the AC-LA pathway, as TL-LA synapses displayed normal LTD (Fig. 6*h*,*i*).

Pten-ΔPDZ Mice Are Impaired Exclusively in Social Interaction

In order to assess the relevance of PDZ-dependent actions of PTEN for cognitive performance, we started testing memory

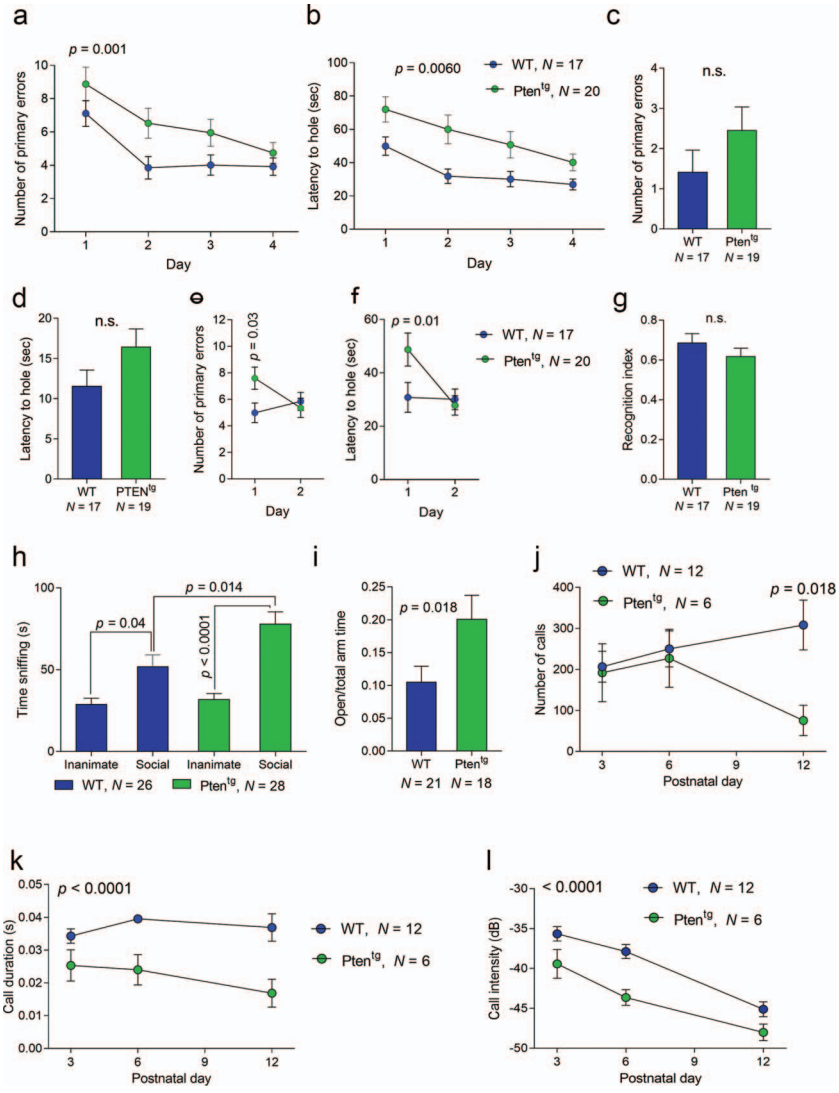

Figure 5. Cognitive performance in Pten^{tg} mice. (*a*) Total primary errors to find the escape hole in a Barnes maze for each day of the experiment (represented as blocks of 4 trials). A 2-way ANOVA revealed a nonsignificant ($P = 0.70$) 2-way interaction for the number of primary errors (day by genotype $F = 0.47$, DFn = 3, DFd = 140). The effect of the genotype was significant ($P = 0.001$, $F = 10.71$, DFn = 3, DFd = 140), as was the effect of the day ($P < 0.0001$, $F = 8.70$, DFn = 3, DFd = 140). (*b*) The latency to find the escape hole in a Barnes maze for each day of the experiment (represented as blocks of 4 trials). A 2-way ANOVA revealed a nonsignificant ($P = 0.44$) 2-way interaction for latency to find the hole (day by genotype $F = 0.91$, DFn = 3, DFd = 105). The effect of the genotype was significant ($P = 0.0060$, $F = 8.56$, DFn = 1, DFd = 35), as was the effect of the day ($P < 0.0001$, $F = 13.32$, DFn = 3, DFd = 105). (*c*) The number of errors to find the covered escape hole during the probe test performed on the fifth day of Barnes maze training: *P* value was determined with a Mann–Whitney test ($P = 0.6$, $F = 1.343$, DFn = 19, DFd = 16), and *N* represents the number of mice. (*d*) The latency to find the covered escape hole during the probe test on the fifth day of Barnes maze training: *P* value was determined with a Mann–Whitney test ($P = 0.07$, $F = 1.396$, DFn = 18, DFd = 16), and *N* represents the number of mice. (*e*) Number of errors to find the new location of the escape hole during the reversal test: *P* value was determined for the first day with a Mann–Whitney test ($F = 1.539$, DFn = 19, Dfd = 16), and *N* represents the number of mice. (*f*) Latency to find the new location of the escape hole during the reversal test: *P* value was determined for the first day with a Mann–Whitney test ($F = 1.463$, DFn = 19, Dfd = 16) and *N* represents the number of mice. (*g*) Recognition index in the novel object location task, calculated as the time exploring the object moved to a new location over the time exploring both objects: *P* value was determined with a Mann–Whitney test ($P = 0.32$, F = 1.099, DFn = 16, Dfd = 18), and *N* represents the number of mice. (*h*) Time spent exploring the social or inanimate target, where *N* represents the number of mice. A 2-way ANOVA revealed a nonsignificant ($P = 0.053$) 2-way interaction for time spent sniffing (subject by genotype, $F = 3.82$, DFn = 1, DFd = 104). The effect of the genotype was significant ($P = 0.016$, $F = 6.00$, DFn = 1, DFd = 104), as was the effect of the subject ($P < 0.0001$, $F = 34.50$, DFn = 1, DFd = 104). *P* values on the graph were determined with Sidak's multiple comparisons tests. (*i*) The ratio of the time spent in the open arm to the time spent in both arms (total arm time), where *N* represents the number of mice and the *P* value was determined with a 2-tailed Mann–Whitney test ($F = 1.920$, DFn = 17, Dfd = 20). (*j*) Total number of USVs (calls) emitted. A 2-way ANOVA revealed a nonsignificant ($P = 0.11$) 2-way interaction for call (day by genotype $F = 2.31$, DFn = 2, DFd = 48). The effect of the genotype was significant only at day 12 ($P = 0.018$, DFd = 48, Sidak's multiple comparisons test). The effect of the day alone was nonsignificant ($P = 0.68$, $F = 0.37$, DFn = 2, DFd = 48). (*k*) The duration of each individual call. A 2-way ANOVA revealed a significant ($P = 0.026$) 2-way interaction for call duration (day by genotype $F = 2.50$, DFn = 6, DFd = 106). The effect of the genotype was significant ($P < 0.0001$, $F = 10.78$, DFn = 3, DFd = 106), as was the effect of the day ($P = 0.0012$, $F = 7.15$, DFn = 2, DFd = 106). (*l*) The intensity of each individual call. A 2-way ANOVA revealed a nonsignificant ($P = 0.432$) 2-way interaction for call intensity (day by genotype $F = 0.85$, DFn = 2, DFd = 48). The effect of the genotype was significant ($P < 0.0001$, $F = 20.52$, DFn = 1, DFd = 48), as was the effect of the day ($P < 0.0001$, $F = 33.66$, DFn = 2, DFd = 48). The data in all graphs are the mean ± s.e.m.

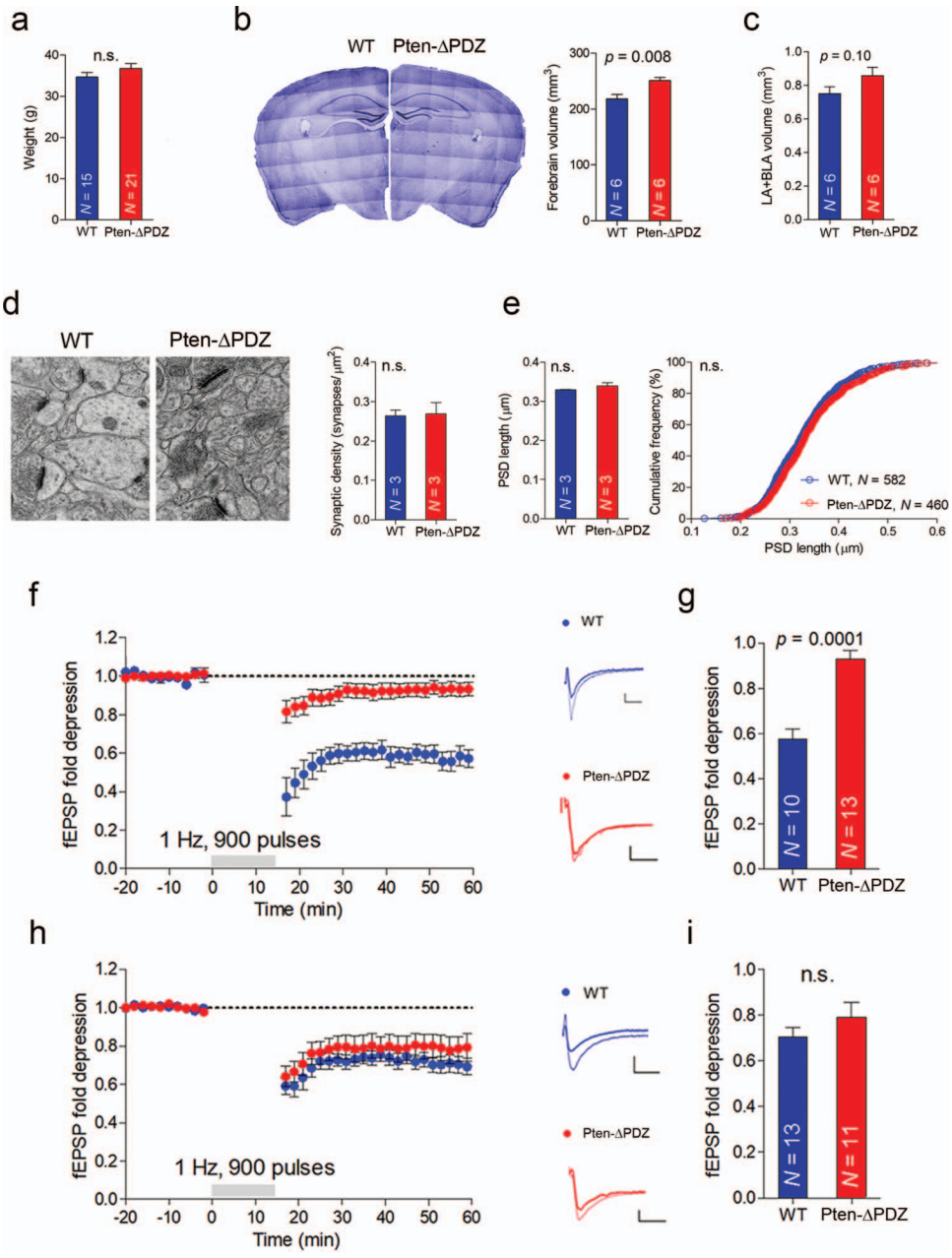

Figure 6. Alterations in brain structure and synaptic function in Pten-ΔPDZ mice. (*a*) Weight of the WT and PTEN-ΔPDZ mice used in this study (*N* represents the number of mice). *P* values was determined with a Mann–Whitney test ($P = 0.20$, $F = 1.796$, DFn = 20, Dfd = 14), and *N* represents the number of mice. (*b*) Left, representative Nissl-stained coronal sections of hemispheres from WT and Pten-ΔPDZ mice obtained using a 40× objective and tile scanned. Right, bar graph showing the forebrain volume. *P* values was determined with a Mann–Whitney test ($F = 2.149$, DFn = 5, Dfd = 5), and *N* represents the number of mice. (*c*) The volume of the LA + BLA determined by unbiased stereology on Nissl-stained preparations. *P* values was determined with a Mann–Whitney test ($F = 1.485$, DFn = 5, Dfd = 5), and *N* represents the number of mice. (*d*) Left, representative electron micrographs depicting the neuropil of the LA, including the pre- and postsynaptic compartments of WT and Pten-ΔPDZ. Right, quantification of the synaptic density. *P* value was determined with a Mann–Whitney test ($P > 0.999$, $F = 4.201$, DFn = 2, Dfd = 2), and *N* represents the number of mice. (*e*) Left, the length of the PSD in LA synapses. *P* values was determined with a Mann–Whitney test ($P > 0.999$, $F = 44.54$, DFn = 2, Dfd = 2), and *N* represents the number of mice. Right, cumulative frequency of the PSD lengths, where *N* represents the number of synapses and the *P* value was determined with a Kolmogorov–Smirnov test. (*f* and *h*) Left, NMDAR-dependent LTD was induced in the LA in coronal slices taken from WT or Pten-ΔPDZ mice (900 pulses at 1 Hz) stimulating axons arising from the auditory cortex (*f*) or thalamus (*h*). Right, representative fEPSPs before (thin line) and after (thick line) LTD induction: scale bars represent 0.5 mV, 20 ms. (*g*) Quantification of the average fEPSP maximal slopes 50–60 min after induction (AC-LA pathway), relative to baseline response. The *P* value was determined with a Mann–Whitney test ($F = 1.277$, DFn = 9, Dfd = 12), and *N* represents the number of mice. (*i*) Quantification of the average fEPSP maximal slopes 50–60 min after induction (TL-LA pathway), relative to baseline response. The *P* value was determined with a Mann–Whitney test ($P = 0.33$, $F = 2.219$, DFn = 10, Dfd = 12), and *N* represents the number of mice. The data in all the graphs are represented as the mean ± s.e.m.

for fear conditioning in Pten-ΔPDZ and WT mice. As described above, this is a form of associative learning in which a neutral stimulus (an auditory cue delivered in a given spatial context) is associated with an aversive event (an electric shock). As shown in Figure 7*a*,*b*, fear response (freezing) was similar in WT and Pten-ΔPDZ animals when exposed to the auditory cue (cued conditioning; panel a) or when present in the same spatial context where the electric shock was delivered (contextual conditioning; panel b). These results imply that fear memory retrieval is not affected in Pten-ΔPDZ animals.

We then tested autistic-related behaviors in these animals, since they represent a form of PTEN deficiency. As shown in Figure 7*c* (two right-most columns), and in contrast to WT animals (two left-most columns), Pten-ΔPDZ mice did not display any preference for the social target over the inanimate object in the 3 chamber apparatus. These results imply that social interactions are dramatically impaired in Pten-ΔPDZ mice. Interestingly, these animals did not present an anxiety-like behavior, as compared to WT, in the EPM (Fig. 7*d*). Likewise, USVs elicited by maternal separation were similar between Pten-ΔPDZ and WT animals (Fig. 7*e*–*g*).

In conclusion, the lack of PDZ interactions of PTEN produced a rather restricted behavioral phenotype, namely, the ablation of social preference, without behavioral symptoms of anxiety. Given the opposite phenotypes of Pten^{tg} and Pten-ΔPDZ mice with respect to AC-LA LTD and social interactions, these results support the notion that the intensity of the activity in the AC-LA circuit and its capacity to undergo synaptic depression are correlated with social behavior.

Discussion

We have addressed the role of PTEN in defining the circuits and synaptic mechanisms that control cognitive function and particularly social behavior. To this end, we have used 2 transgenic mouse lines that exhibit opposite phenotypes in several critical aspects. First, mice that overexpress PTEN (Pten^{tg} mice) show exaggerated levels of LTD in the AC-LA pathway and intensified social interactions. In contrast, mice with a partial PTEN loss-of-function (Pten-ΔPDZ) exhibit impaired LTD in the AC-LA pathway and virtually abolished social preference. Therefore, these combined data suggest that in addition to controlling brain size, PTEN may determine the extent of social behavior in part by modulating the plasticity (or flexibility) of specific neuronal circuits.

PTEN overexpression did produce pleiotropic effects on brain structure and function. Arguably, some of the phenotypes of Pten^{tg} mice, such as microcephaly, reduced neuronal size, and synaptic density, are related to the role of PTEN in growth control. Interestingly, brain region- and circuit-specific alterations may still be observed upon manipulation of a general growth regulator, such as PTEN, probably as a consequence of desynchronized phases of neuronal growth (Huang et al. 2016). Nevertheless, other phenotypes of these animals are probably more directly linked to PTEN's action at synapses, such as attenuated synaptic plasticity signaling or impaired LTP expression (in both hippocampus and amygdala). These effects may well be related to the impaired spatial learning and fear memory retrieval in these animals. This consideration was the main driver to study the Pten-ΔPDZ mice. This genetic mouse model bears a modification in PTEN particularly designed to alter mostly its synaptic function (Jurado et al. 2010; Knafo et al. 2016), even though additional alterations in growth control cannot be discounted. Thus, the restricted behavioral phenotype of these animals, namely impaired social preference, may be a consequence of lacking PTEN activity at synapses, even if this deficit in turn may impinge on postnatal developmental programs. This interpretation is supported by the bidirectional correlation between LTD at AC-LA synapses and social behavior in Pten^{tg} and Pten-ΔPDZ mice, as mentioned above. Importantly, other morphological, physiological, or behavioral parameters of these animal models do not display this opposing pattern. For example, synapse density and basal transmission are both reduced in Pten^{tg} mice. This result is consistent with the hyperconnectivity and hyperactivity previously reported for the basolateral amygdala of heterozygous PTEN KO mice (*Pten*$^{+/-}$) (Huang et al. 2016). However, it is in contrast with the normal (similar to WT) synaptic density and basal transmission we have observed in Pten-ΔPDZ mice. Also, anxiety-like behavior is attenuated in Pten^{tg} mice (our results) and it is enhanced in animals deficient in global PTEN activity (Kwon et al. 2006; Lugo et al. 2014). However, anxiety levels are normal (not enhanced) in Pten-ΔPDZ mice. These considerations strengthen the correlation between the capacity to undergo LTD and social behavior. Obviously, we are not claiming that this form of synaptic plasticity is solely responsible for social preference, as this is a complex behavior known to engage multiple brain circuits, such as those involving ventral tegmental area, prefrontal cortex, hippocampus, and cerebellum (Santini et al. 2013; Wang et al. 2014a, 2014b; Bariselli et al. 2016; Huang et al. 2016; Chen and Hong 2018; Del Pino et al. 2018). Nevertheless, we would propose that synaptic plasticity at specific amygdala circuits is a contributing factor to gage the propensity for social interaction.

It is also worth noting that communication and social problems are core features of autistic patients with PTEN loss-of-function mutations (PTEN-ASD) (Zhou and Parada 2012). The fact that synaptic dysfunctions may underlie neurodevelopmental disorders, including ASD, has been appreciated before (see some reviews [Zoghbi 2003; Bourgeron 2009; Spooren et al. 2012; Zoghbi and Bear 2012; Bourgeron 2015; Knafo and Esteban 2017]). In this sense, a specific synaptic dysfunction (such as the failure to depress or tone down synaptic communication) may provide a common pathway for multiple genetic components to converge. Thus, several ASD-associated mutations upregulate Ras-MAPK and PI3K-mTOR pathways, promoting synaptic growth and potentiation (Opazo et al. 2003; Kelleher et al. 2004; Thomas and Huganir 2004; Qin et al. 2005; Hoeffer and Klann 2010; Buffington et al. 2014; Huber et al. 2015; Huang *et al*. 2016; Borrie et al. 2017). In this manner, they are likely to interfere with physiological synaptic depression, as PTEN deficiency does. This interpretation also fits well with the parallelisms between synaptic depression and developmental synaptic pruning (Piochon et al. 2016), which is also thought to be defective in ASD (Hansel 2018). Importantly, this argument may blur the distinction between developmental and synaptic effects of PTEN. Thus, a defective mechanism for synaptic depression during early postnatal development may produce an overabundance of prematurely stabilized synapses, which would be less likely to be removed, leading to hyperconnectivity. In fact, this phenotype has been observed in autistic children (Di Martino et al. 2011; Supekar et al. 2013) and in animal models of ASD with altered synaptic scaffolding molecules (Gkogkas et al. 2013; Peixoto et al. 2016).

Finally, it is intriguing that enhancement of PTEN activity at synapses (by overexpression) produces supraphysiological

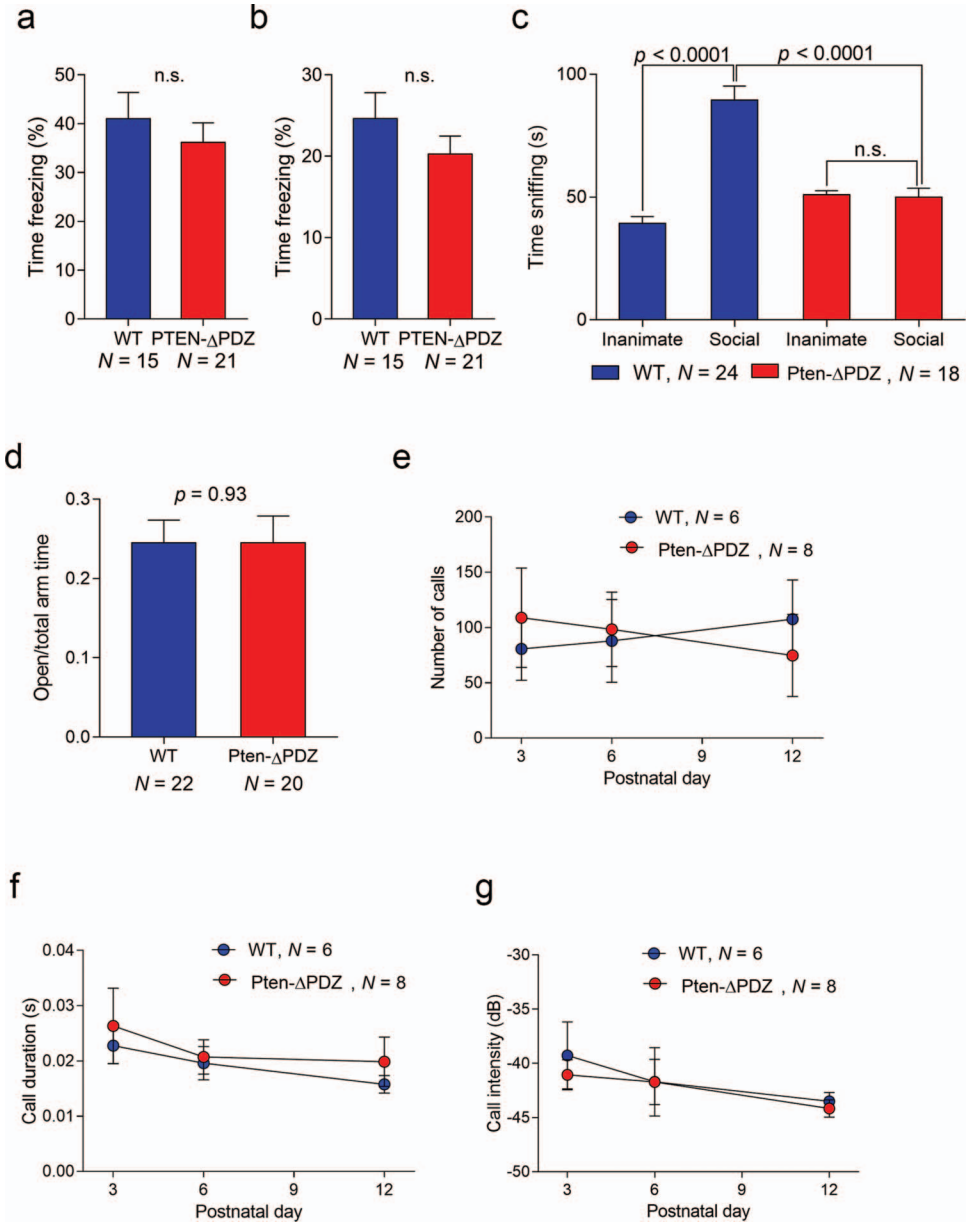

Figure 7. Cognitive performance in Pten-ΔPDZ mice. (*a*) Freezing during the exposure to the auditory cue and 24 h after training for cued fear conditioning; *P* value was determined with Mann–Whitney test ($P = 0.22$, $F = 2.796$, DFn = 9, Dfd = 10), and *N* represents the number of mice. (*b*) Freezing during a 5 min exposure to the context and 24 h after training for contextual fear conditioning: *P* value was determined with Mann–Whitney test ($P = 0.55$, $F = 1.672$, DFn = 9, Dfd = 10), and *N* represents the number of mice. (*c*) Time spent exploring the social or inanimate target in the 3-chamber apparatus, where *N* represents the number of mice. A 2-way ANOVA revealed a significant ($P < 0.0001$) 2-way interaction for time spent sniffing (subject by genotype $F = 40.44$, DFn = 1, DFd = 80). The effect of the genotype was significant ($P = 0.0009$, $F = 11.84$, DFn = 1, DFd = 80), as was the effect of the subject ($P < 0.0001$, $F = 37.47$, DFn = 1, DFd = 80). *P* values on the graph were determined with Sidak's multiple comparisons tests. (*d*) The ratio of the time spent in the open arm to the time spent in both arms (total arm time) in the EPM, where *N* represents the number of mice and the *P* value was determined with a 2-tailed Mann–Whitney test ($F = 1.259$, DFn = 19, Dfd = 21). (*e*) Total number of USVs (calls) emitted. A 2-way ANOVA revealed a nonsignificant ($P = 0.70$) 2-way interaction for call (day by genotype $F = 0.36$, DFn = 2, DFd = 34). The effect of the genotype was not significant either ($P = 0.95$, $F = 0.3.86e\text{-}003$, DFn = 1, DFd = 34). The effect of the day was nonsignificant ($P = 0.995$, $F = 4.58e\text{-}003$, DFn = 2, DFd = 34). (*f*) The duration of each individual call. A 2-way ANOVA revealed a nonsignificant ($P = 0.933$) 2-way interaction for call (day by genotype $F = 0.07$, DFn = 2, DFd = 31). The effect of the genotype was not significant either ($P = 0.416$, $F = 0.68$, DFn = 1, DFd = 31). The effect of the day was nonsignificant ($P = 0.31$, $F = 1.21$, DFn = 2, DFd = 31). (*g*) The intensity of each individual call. A 2-way ANOVA revealed a nonsignificant ($P = 0.972$) 2-way interaction for call intensity (day by genotype $F = 0.08$, DFn = 3, DFd = 42). The effect of the genotype was nonsignificant ($P = 0.610$, $F = 0.26$, DFn = 1, DFd = 42), as was the effect of the day ($P = 0.21$, $F = 1.57$, DFn = 3, DFd = 42).The data in all graphs are the mean ± s.e.m.

changes in social preference. These results suggest that the PI3K/PTEN pathway represents a continuous axis that defines basic properties of synaptic modulation during development, with bidirectional outcomes for social behavior.

Funding

Spanish Ministry of Economy and Competitiveness (SAF2016-78071-R and SAF2015-62540-ERC to S.K.; PCIN-2016-095 and SAF2017-86983-R to J.A.E.; BFU201563769-R to R.L.; SAF2014-58598-JIN and RYC-2016-20414 to M.N.); Basque Ministry of Health (RIS3 and ELKARTEK to S.K.); University of the Basque Country (EHUrOPE14/03 to S.K.); Junta de Comunidades de Castilla–La Mancha (PPII2014-005-P to R.L.); Spanish Ministry of Economy and Competitiveness (BES-2011-043464 to C.S.-P.).

Notes

The Pten^{tg} mice were generated and generously provided by Manuel Serrano (IRB, Barcelona, Spain). We thank Dr Francisca Mulero (CNIO, Madrid) for her help with CT-PET imaging. We also thank Yann Humeau for initial assistance with the amygdala electrophysiology recordings. *Conflict of Interest*: None declared.

Author Contributions

C.S.-P. performed most of the experiments under the supervision of S.K. and J.A.E. M.C.-F., G.B., M.N., and A.A. performed some of the experiments. J.M.H. analyzed the EM data under the supervision of R.L. A.A. analyzed some of the EM data under the supervision of S.K. A.E. and I.D. analyzed the CT and PET data under the supervision of J.C. C.V. designed and supervised all the behavioral experiments. M.M. performed experiments and supervised students. C.S.-P., J.A.E., and S.K. wrote the paper.

References

Aincy M, Meziane H, Herault Y, Humeau Y. 2018. Synaptic dysfunction in amygdala in intellectual disorder models. *Prog Neuropsychopharmacol Biol Psychiatry*. 84:392–397.

Amiri A, Cho W, Zhou J, Birnbaum SG, Sinton CM, McKay RM, Parada LF. 2012. Pten deletion in adult hippocampal neural stem/progenitor cells causes cellular abnormalities and alters neurogenesis. *J Neurosci*. 32:5880–5890.

Arendt KL, Benoist M, Lario A, Draffin JE, Munoz M, Esteban JA. 2014. PTEN counteracts PIP3 upregulation in spines during NMDA-receptor-dependent long-term depression. *J Cell Sci*. 127:5253–5260.

Arendt KL, Royo M, Fernandez-Monreal M, Knafo S, Petrok CN, Martens JR, Esteban JA. 2010. PIP3 controls synaptic function by maintaining AMPA receptor clustering at the postsynaptic membrane. *Nat Neurosci*. 13:36–44.

Bai J, Trinh TLH, Chuang KH, Qiu A. 2012. Atlas-based automatic mouse brain image segmentation revisited: model complexity vs. image registration. *Magn Reson Imaging*. 30:789–798.

Bariselli S, Tzanoulinou S, Glangetas C, Prevost-Solie C, Pucci L, Viguie J, Bezzi P, O'Connor EC, Georges F, Luscher C *et al*. 2016. SHANK3 controls maturation of social reward circuits in the VTA. *Nat Neurosci*. 19:926–934.

Barnes CA. 1979. Memory deficits associated with senescence: A neurophysiological and behavioral study in the rat. *J Comp Physiol Psychol*. 93:74–104.

Barria A, Muller D, Derkach V, Griffith LC, Soderling TR. 1997. Regulatory phosphorylation of AMPA-type glutamate receptors by CaM-KII during long-term potentiation. *Science*. 276:2042–2045.

Blair RJ. 2013. The neurobiology of psychopathic traits in youths. *Nat Rev Neurosci*. 14:786–799.

Blasco B, Avendaño C, Cavada C. 1999. A stereological analysis of the lateral geniculate nucleus in adult Macaca nemestrina monkeys. *Vis Neurosci*. 16:933–941.

Borrie SC, Brems H, Legius E, Bagni C. 2017. Cognitive dysfunctions in intellectual disabilities: the contributions of the Ras-MAPK and PI3K-AKT-mTOR pathways. *Annu Rev Genomics Hum Genet*. 18:115–142.

Bourgeron T. 2009. A synaptic trek to autism. *Curr Opin Neurobiol*. 19:231–234.

Bourgeron T. 2015. From the genetic architecture to synaptic plasticity in autism spectrum disorder. *Nat Rev Neurosci*. 16:551–563.

Buffington SA, Huang W, Costa-Mattioli M. 2014. Translational control in synaptic plasticity and cognitive dysfunction. *Annu Rev Neurosci*. 37:17–38.

Cai QY, Chen XS, Zhong SC, Luo X, Yao ZX. 2009. Differential expression of PTEN in normal adult rat brain and upregulation of PTEN and p-Akt in the ischemic cerebral cortex. *Anat Rec (Hoboken)*. 292:498–512.

Cantley LC. 2002. The phosphoinositide 3-kinase pathway. *Science*. 296:1655–1657.

Chen P, Hong W. 2018. Neural circuit mechanisms of social behavior. *Neuron*. 98:16–30.

Chow DK, Groszer M, Pribadi M, Machniki M, Carmichael ST, Liu X, Trachtenberg JT. 2009. Laminar and compartmental regulation of dendritic growth in mature cortex. *Nat Neurosci*. 12:116–118.

Crawley JN. 2004. Designing mouse behavioral tasks relevant to autistic-like behaviors. *Ment Retard Dev Disabil Res Rev*. 10:248–258.

Cuesto G, Enriquez-Barreto L, Carames C, Cantarero M, Gasull X, Sandi C, Ferrus A, Acebes A, Morales M. 2011. Phosphoinositide-3-kinase activation controls synaptogenesis and spinogenesis in hippocampal neurons. *J Neurosci*. 31:2721–2733.

Del Pino I, Rico B, Marin O. 2018. Neural circuit dysfunction in mouse models of neurodevelopmental disorders. *Curr Opin Neurobiol*. 48:174–182.

Di Martino A, Kelly C, Grzadzinski R, Zuo XN, Mennes M, Mairena MA, Lord C, Castellanos FX, Milham MP. 2011. Aberrant striatal functional connectivity in children with autism. *Biol Psychiatry*. 69:847–856.

Fanselow MS, Dong HW. 2010. Are the dorsal and ventral hippocampus functionally distinct structures. *Neuron*. 65:7–19.

Frazier TW, Embacher R, Tilot AK, Koenig K, Mester J, Eng C. 2015. Molecular and phenotypic abnormalities in individuals with germline heterozygous PTEN mutations and autism. *Mol Psychiatry*. 20:1132–1138.

Garcia-Cao I, Song MS, Hobbs RM, Laurent G, Giorgi C, de Boer VC, Anastasiou D, Ito K, Sasaki AT, Rameh L *et al*. 2012. Systemic elevation of PTEN induces a tumor-suppressive metabolic state. *Cell*. 149:49–62.

Gkogkas CG, Khoutorsky A, Ran I, Rampakakis E, Nevarko T, Weatherill DB, Vasuta C, Yee S, Truitt M, Dallaire P *et al*. 2013. Autism-related deficits via dysregulated eIF4E-dependent translational control. *Nature*. 493:371–377.

González-Fernández E, Jeong HK, Fukaya M, Kim H, Khawaja RR, Srivastava IN, Waisman A, Son YJ, Kang SH. 2018. PTEN negatively regulates the cell lineage progression from NG2$^+$ glial progenitor to oligodendrocyte via mTOR-independent signaling. *Elife*. 7:e32021.

Gregorian C, Nakashima J, Le Belle J, Ohab J, Kim R, Liu A, Smith KB, Groszer M, Garcia AD, Sofroniew MV *et al*. 2009. Pten deletion in adult neural stem/progenitor cells enhances constitutive neurogenesis. *J Neurosci*. 29:1874–1886.

Hansel C. 2019. Deregulation of synaptic plasticity in autism. *Neurosci Lett*. 688:58–61.

Heckman J, McGuinness B, Celikel T, Englitz B. 2016. Determinants of the mouse ultrasonic vocal structure and repertoire. *Neurosci Biobehav Rev*. 65:313–325.

Hoeffer CA, Klann E. 2010. mTOR signaling: at the crossroads of plasticity, memory and disease. *Trends Neurosci*. 33:67–75.

Huang WC, Chen Y, Page DT. 2016. Hyperconnectivity of prefrontal cortex to amygdala projections in a mouse model of macrocephaly/autism syndrome. *Nat Commun*. 7:13421.

Huber KM, Klann E, Costa-Mattioli M, Zukin RS. 2015. Dysregulation of mammalian target of rapamycin signaling in mouse models of autism. *J Neurosci*. 35:13836–13842.

Hunsaker MR, Kesner RP. 2008. Dissociations across the dorsal–ventral axis of CA3 and CA1 for encoding and retrieval of contextual and auditory-cued fear. *Neurobiol Learn Mem*. 89:61–69.

Jenkinson M, Smith S. 2001. A global optimisation method for robust affine registration of brain images. *Med Image Anal*. 5:143–156.

Jurado S, Benoist M, Lario A, Knafo S, Petrok CN, Esteban JA. 2010. PTEN is recruited to the postsynaptic terminal for NMDA receptor-dependent long-term depression. *EMBO J*. 29:2827–2840.

Kelleher RJ 3rd, Govindarajan A, Jung HY, Kang H, Tonegawa S. 2004. Translational control by MAPK signaling in long-term synaptic plasticity and memory. *Cell*. 116:467–479.

Kim JJ, Jung MW. 2006. Neural circuits and mechanisms involved in Pavlovian fear conditioning: a critical review. *Neurosci Biobehav Rev*. 30:188–202.

Knafo S, Alonso-Nanclares L, Gonzalez-Soriano J, Merino-Serrais P, Fernaud-Espinosa I, Ferrer I, DeFelipe J. 2009a. Widespread changes in dendritic spines in a model of Alzheimer's disease. *Cereb Cortex*. 19:586–592.

Knafo S, Esteban JA. 2017. PTEN: local and global modulation of neuronal function in health and disease. *Trends Neurosci*. 40:83–91.

Knafo S, Sanchez-Puelles C, Palomer E, Delgado I, Draffin JE, Mingo J, Wahle T, Kaleka K, Mou L, Pereda-Perez I *et al*. 2016. PTEN recruitment controls synaptic and cognitive function in Alzheimer's models. *Nat Neurosci*. 19:443–453.

Knafo S, Venero C, Merino-Serrais P, Fernaud-Espinosa I, Gonzalez-Soriano J, Ferrer I, Santpere G, DeFelipe J. 2009b. Morphological alterations to neurons of the amygdala and impaired fear conditioning in a transgenic mouse model of Alzheimer's disease. *J Pathol*. 219:41–51.

Kwon CH, Luikart BW, Powell CM, Zhou J, Matheny SA, Zhang W, Li Y, Baker SJ, Parada LF. 2006. Pten regulates neuronal arborization and social interaction in mice. *Neuron*. 50:377–388.

Li J, Yen C, Liaw D, Podsypanina K, Bose S, Wang SI, Puc J, Miliaresis C, Rodgers L, McCombie R *et al*. 1997. PTEN, a putative protein tyrosine phosphatase gene mutated in human brain, breast, and prostate cancer. *Science*. 275:1943.

Li X, Aggarwal M, Hsu J, Jiang H, Mori S. 2013. AtlasGuide: software for stereotaxic guidance using 3D CT/MRI hybrid atlases of developing mouse brains. *J Neurosci Methods*. 220:75–84.

Liaw D, Marsh DJ, Li J, Dahia PL, Wang SI, Zheng Z, Bose S, Call KM, Tsou HC, Peacocke M *et al*. 1997. Germline mutations of the PTEN gene in Cowden disease, an inherited breast and thyroid cancer syndrome. *Nat Genet*. 16:64–67.

Lisman J, Yasuda R, Raghavachari S. 2012. Mechanisms of CaMKII action in long-term potentiation. *Nat Rev Neurosci*. 13:169–182.

Lu W, Man H, Ju W, Trimble WS, MacDonald JF, Wang YT. 2001. Activation of synaptic NMDA receptors induces membrane insertion of new AMPA receptors and LTP in cultured hippocampal neurons. *Neuron*. 29:243–254.

Lugo JN, Smith GD, Arbuckle EP, White J, Holley AJ, Floruta CM, Ahmed N, Gomez MC, Okonkwo O. 2014. Deletion of PTEN produces autism-like behavioral deficits and alterations in synaptic proteins. *Front Mol Neurosci*. 7:27.

Luikart BW, Schnell E, Washburn EK, Bensen AL, Tovar KR, Westbrook GL. 2011. Pten knockdown in vivo increases excitatory drive onto dentate granule cells. *J Neurosci*. 31:4345–4354.

Magistretti PJ, Pellerin L. 1999. Cellular mechanisms of brain energy metabolism and their relevance to functional brain imaging. *Philos Trans R Soc Lond B Biol Sci*. 354:1155.

Mammen AL, Kameyama K, Roche KW, Huganir RL. 1997. Phosphorylation of the alpha-amino-3-hydroxy-5-methylisoxazole4-propionic acid receptor GluR1 subunit by calcium/calmodulin-dependent kinase II. *J Biol Chem*. 272:32528–32533.

Man HY, Wang Q, Lu WY, Ju W, Ahmadian G, Liu L, D'Souza S, Wong TP, Taghibiglou C, Lu J *et al*. 2003. Activation of PI3-kinase is required for AMPA receptor insertion during LTP of mEPSCs in cultured hippocampal neurons. *Neuron*. 38:611–624.

Maren S, Quirk GJ. 2004. Neuronal signalling of fear memory. *Nat Rev Neurosci*. 5:844–852.

Opazo P, Watabe AM, Grant SG, O'Dell TJ. 2003. Phosphatidylinositol 3-kinase regulates the induction of long-term potentiation through extracellular signal-related kinase-independent mechanisms. *J Neurosci*. 23:3679–3688.

Ortega-Molina A, Efeyan A, Lopez-Guadamillas E, Munoz-Martin M, Gomez-Lopez G, Canamero M, Mulero F, Pastor J, Martinez S, Romanos E *et al*. 2012. Pten positively regulates brown adipose function, energy expenditure, and longevity. *Cell Metab*. 15:382–394.

Passafaro M, Piëch V, Sheng M. 2001. Subunit-specific temporal and spatial patterns of AMPA receptor exocytosis in hippocampal neurons. *Nat Neurosci*. 4:917.

Paz R, Pare D. 2013. Physiological basis for emotional modulation of memory circuits by the amygdala. *Curr Opin Neurobiol*. 23:381–386.

Peineau S, Taghibiglou C, Bradley C, Wong TP, Liu L, Lu J, Lo E, Wu D, Saule E, Bouschet T *et al*. 2007. LTP inhibits LTD in the hippocampus via regulation of GSK3beta. *Neuron*. 53: 703–717.

Peixoto RT, Wang W, Croney DM, Kozorovitskiy Y, Sabatini BL. 2016. Early hyperactivity and precocious maturation of corticostriatal circuits in Shank3B(−/−) mice. *Nat Neurosci*. 19:716–724.

Perandones C, Costanzo RV, Kowaljow V, Pivetta OH, Carminatti H, Radrizzani M. 2004. Correlation between synaptogenesis and the PTEN phosphatase expression in dendrites during postnatal brain development. *Brain Res Mol Brain Res*. 128:8–19.

Piochon C, Kano M, Hansel C. 2016. LTD-like molecular pathways in developmental synaptic pruning. *Nat Neurosci*. 19:1299–1310.

Pun Raymund YK, Rolle Isaiah J, LaSarge Candi L, Hosford Bethany E, Rosen Jules M, Uhl Juli D, Schmeltzer Sarah N, Faulkner C, Bronson Stefanie L, Murphy Brian L *et al*. 2012. Excessive activation of mTOR in postnatally generated granule cells is sufficient to cause epilepsy. *Neuron*. 75:1022–1034.

Qin Y, Zhu Y, Baumgart JP, Stornetta RL, Seidenman K, Mack V, van Aelst L, Zhu JJ. 2005. State-dependent Ras signaling and AMPA receptor trafficking. *Genes Dev*. 19: 2000–2015.

Rogan MT, Staubli UV, LeDoux JE. 1997. Fear conditioning induces associative long-term potentiation in the amygdala. *Nature*. 390:604–607.

Rumpel S, LeDoux J, Zador A, Malinow R. 2005. Postsynaptic receptor trafficking underlying a form of associative learning. *Science*. 308:83–88.

Santini E, Huynh TN, MacAskill AF, Carter AG, Pierre P, Ruggero D, Kaphzan H, Klann E. 2013. Exaggerated translation causes synaptic and behavioural aberrations associated with autism. *Nature*. 493:411–415.

Silverman JL, Yang M, Lord C, Crawley JN. 2010. Behavioural phenotyping assays for mouse models of autism. *Nat Rev Neurosci*. 11:490–502.

Sperow M, Berry RB, Bayazitov IT, Zhu G, Baker SJ, Zakharenko SS. 2012. Phosphatase and tensin homologue (PTEN) regulates synaptic plasticity independently of its effect on neuronal morphology and migration. *J Physiol*. 590: 777–792.

Spooren W, Lindemann L, Ghosh A, Santarelli L. 2012. Synapse dysfunction in autism: a molecular medicine approach to drug discovery in neurodevelopmental disorders. *Trends Pharmacol Sci*. 33:669–684.

Stiles B, Groszer M, Wang S, Jiao J, Wu H. 2004. PTENless means more. *Dev Biol*. 273:175–184.

Supekar K, Uddin LQ, Khouzam A, Phillips J, Gaillard WD, Kenworthy LE, Yerys BE, Vaidya CJ, Menon V. 2013. Brain hyperconnectivity in children with autism and its links to social deficits. *Cell Rep*. 5:738–747.

Takeuchi K, Gertner MJ, Zhou J, Parada LF, Bennett MV, Zukin RS. 2013. Dysregulation of synaptic plasticity precedes appearance of morphological defects in a Pten conditional knockout mouse model of autism. *Proc Natl Acad Sci U S A*. 110:4738–4743.

Thomas GM, Huganir RL. 2004. MAPK cascade signalling and synaptic plasticity. *Nat Rev Neurosci*. 5:173–183.

Wang F, Kessels HW, Hu H. 2014b. The mouse that roared: neural mechanisms of social hierarchy. *Trends Neurosci*. 37:674–682.

Wang SS, Kloth AD, Badura A. 2014a. The cerebellum, sensitive periods, and autism. *Neuron*. 83:518–532.

Wang Y, Cheng A, Mattson MP. 2006. The PTEN phosphatase is essential for long-term depression of hippocampal synapses. *Neuromolecular Med*. 8:329–336.

White SW, Oswald D, Ollendick T, Scahill L. 2009. Anxiety in children and adolescents with autism spectrum disorders. *Clin Psychol Rev*. 29:216–229.

Williams MR, DeSpenza T Jr, Li M, Gulledge AT, Luikart BW. 2015. Hyperactivity of newborn Pten knock-out neurons results from increased excitatory synaptic drive. *J Neurosci*. 35:943–959.

Yan M, Wang Y, Wong CW, Or PM, Wong KL, Li L, Many AM, Guan H, Khoo US, Chan AM. 2018. PTEN PDZ-binding domain suppresses mammary carcinogenesis in the MMTV-PyMT breast cancer model. *Cancer Lett*. 430:67–78.

Yeung KS, Tso WWY, Ip JJK, Mak CCY, Leung GKC, Tsang MHY, Ying D, Pei SLC, Lee SL, Yang W *et al*. 2017. Identification of mutations in the PI3K-AKT-mTOR signalling pathway in patients with macrocephaly and developmental delay and/or autism. *Mol Autism*. 8:66.

Zhou J, Parada LF. 2012. PTEN signaling in autism spectrum disorders. *Curr Opin Neurobiol*. 22:873–879.

Zoghbi HY. 2003. Postnatal neurodevelopmental disorders: meeting at the synapse. *Science*. 302:826–830.

Zoghbi HY, Bear MF. 2012. Synaptic dysfunction in neurodevelopmental disorders associated with autism and intellectual disabilities. *Cold Spring Harb Perspect Biol*. 4:a009886.